

# Holographic charge localization at brane intersections

---

Mario Araújo,<sup>a</sup> Daniel Areán,<sup>a</sup> Johanna Erdmenger<sup>a</sup> and Javier M. Lizana<sup>b</sup>

<sup>a</sup>*Max-Planck-Institut für Physik (Werner-Heisenberg-Institut)  
Föhringer Ring 6, D-80805 Munich, Germany*

<sup>b</sup>*CAFPE and Departamento de Física Teórica y del Cosmos  
Universidad de Granada, E-18071 Granada, Spain*

*E-mail:* [maraujo@mpp.mpg.de](mailto:maraujo@mpp.mpg.de), [darean@mpp.mpg.de](mailto:darean@mpp.mpg.de), [jke@mpp.mpg.de](mailto:jke@mpp.mpg.de),  
[jlizan@ugr.es](mailto:jlizan@ugr.es)

**ABSTRACT:** Using gauge/gravity duality, we investigate charge localization near an interface in a strongly coupled system. For this purpose we consider a top-down holographic model and determine its conductivities. Our model corresponds to a holographic interface which localizes charge around a (1+1)-dimensional defect in a (2+1)-dimensional system. The setup consists of a D3/D5 intersection at finite temperature and charge density. We work in the probe limit, and consider massive embeddings of a D5-brane where the mass depends on one of the field theory spatial directions, with a profile interpolating between a negative and a positive value. We compute the conductivity in the direction parallel and perpendicular to the interface. For the latter case we are able to express the DC conductivity as a function of background horizon data. At the interface, the DC conductivity in the parallel direction is enhanced up to five times with respect to that in the orthogonal one. We study the implications of broken translation invariance for the AC and DC conductivities.

**KEYWORDS:** AdS-CFT Correspondence, Gauge-gravity correspondence, Holography and condensed matter physics (AdS/CMT), Intersecting branes models.

---

## Contents

<b>1</b>	<b>Introduction</b>	<b>1</b>
<b>2</b>	<b>Localized charge at brane intersections</b>	<b>5</b>
2.1	Black D3-branes	5
2.2	Probe D5-brane	6
2.2.1	Action and equations of motion	7
2.3	Inhomogeneous embeddings and charge localization	9
2.4	Numerical Results	11
<b>3</b>	<b>Conductivities</b>	<b>13</b>
3.1	Fluctuations	14
3.2	DC conductivity	16
3.3	Numerics	19
3.4	Results	21
3.4.1	DC conductivity	25
<b>4</b>	<b>Conclusions</b>	<b>28</b>
<b>A</b>	<b>Background equations of motion</b>	<b>30</b>
<b>B</b>	<b>Quadratic action for the fluctuations</b>	<b>31</b>

---

## 1 Introduction

The AdS/CFT correspondence [1–4] and its extensions to more general examples of gauge/gravity duality are by now well established as a powerful modeling tool for strongly coupled systems. This applies in particular to systems of relevance for condensed matter physics.

A number of relevant phenomena in condensed matter physics involve the presence of an interface between materials of different kind. Such interfaces represent a localized impurity which breaks translational symmetry in the system. Broken translational symmetry allows the charge carriers to dissipate their momentum. In the case of strong coupling where the standard quasiparticle picture does not apply, many questions about the exact form of this mechanism are still open. Gauge/gravity duality reveals itself as a natural tool to further explore momentum dissipation at strong coupling, given that it provides a method for describing strongly coupled systems by mapping them to weakly coupled gravity theories.

Recently, significant progress has been achieved in studying holographic systems with broken translation invariance by numerically solving the resulting equations of motion,

which are in general partial differential equations (PDEs). These include setups with different holographic realizations of lattices [5–12] through periodically space-dependent sources, and also setups implementing disordered sources [13–16]. Moreover, a lattice realization where PDEs are avoided, which goes under the name of Q-lattices given its resemblance to the construction of Q-balls [17], was introduced in [18] and further explored in [19, 20]. Alternatively to introducing translational symmetry breaking by spatially modulating the sources of conserved currents, momentum relaxation may also be realized by explicitly breaking diffeomorphism invariance in the bulk [21–27], which in [28] led to progress on the study of the conductivity for systems with broken translational symmetry. An example is given by helical lattices [29–33]. Furthermore, translation invariance may also be broken spontaneously [34, 35].

In this paper we consider the breaking of translation invariance by an interface. We consider a top-down model involving a probe brane with a kink geometry. The basic idea is to incorporate the existence of massless modes localized on an interface by letting the embedding vary over one of the boundary coordinates, say  $x$ , in addition to being a function of the radial coordinate. The embedding function asymptotes to a positive value  $m$  (with  $m_q = 2\pi\alpha'm$  the quark mass) for  $x \rightarrow \infty$  and to  $-m$  for  $x \rightarrow -\infty$ , while it vanishes at  $x = 0$ , therefore introducing a defect there. Our work is motivated in part by a model constructed in [36] to holographically realize topological insulators by means of the D3/D7 intersection. This kind of configuration was used in [37] for both D7 and D5 probe branes to verify the expected topologically protected transport properties for (2+1)- and (1+1)-dimensional defects, which are holographic constructions of respectively (2+1)-dimensional Topological Insulators and (1+1)-dimensional Quantum Spin Hall Insulators, see also [38]. The interpretation as a topological insulator arises from the localization of fermions at the interface. In fact, as already shown within field theory in [39, 40], in 3+1 dimensions there are massless localized fermions for a Lagrangian of the form

$$\mathcal{L} = \bar{\psi} (i\cancel{\partial} - m_q(x)) \psi, \quad (1.1)$$

in which  $m_q(x)$  jumps from a positive to a negative value at an interface. The thermodynamic properties of the D7-brane model with a kink [36] were computed in [41], where the PDE equations of motion for the brane embedding in a black D3-brane background were solved, and the relationship between the charge density and the chemical potential was analyzed in connection with the possible fermionic character of the gapless interface excitations. A supersymmetric realization of the D7-brane holographic Topological Insulator model was given in [42].

The present paper relies on the use of probe branes, and therefore past results for these are relevant for explaining the new structures we construct. Hence we briefly review the pertinent features of holographic probe brane intersections. As part of the quest for holographic models of QCD, which requires the presence of fundamental degrees of freedom, probe D-brane systems were the subject of intensive study in the past. By considering  $N_f$  D7-branes embedded in the background generated by  $N$  D3-branes ( $AdS_5 \times S^5$ ) in the limit  $N_f \ll N$ , one can construct the holographic dual of  $\mathcal{N} = 4$   $SU(N)$  SYM with  $N_f$   $\mathcal{N} = 2$  matter hypermultiplets, which are realized by the open strings stretching between

the D3- and D7-branes. The probe D7-branes are therefore called flavor branes [43, 44]. Moreover, a finite temperature is introduced by considering the background generated by black D3-branes, while nonzero quark density, *i.e.* density of the fundamental degrees of freedom, may be added by switching on the temporal component of the worldvolume gauge field on the D7-branes. A similar construction with D5 instead of D7 flavor branes overlapping with the background D3-branes along 2+1 dimensions is dual to  $\mathcal{N} = 4$  SYM with  $\mathcal{N} = 2$  fundamental matter living on a (2+1)-dimensional defect [45–47]. At finite density and magnetic field, these D3/D5 systems display a BKT phase transition [48]. Analyses of finite temperature setups with probe D7-branes [49, 50] and probe D5-branes [51] have established two qualitatively different embeddings: those in which the brane ends before reaching the black hole horizon, denoted Minkowski embeddings, and those in which the brane reaches the horizon, called black hole embeddings. There is a first order phase transition between both types of embedding which has been identified with the melting of mesons in the dual field theory [52]. However, in the presence of a nonzero quark density, only black hole embeddings are possible [53–55].

In this work we consider a D5-brane probing the black D3-brane background. The D5-brane shares 2+1 directions with the D3-branes, and hence gives rise in the dual theory to fundamental matter living on a (2+1)-dimensional defect. Furthermore, the embedding presents a kink-like profile as described above, thus creating a (1+1)-dimensional interface at  $x = 0$ , where the mass of the quarks vanishes. A finite quark density is introduced via the temporal component of the worldvolume gauge field. Since our embeddings are of the black hole kind, this charge density is non-vanishing along the entire system, that is for all  $x$ . There exist however homogeneous black hole embeddings where the charge density is arbitrarily small, so we can engineer kink profiles for our system such that the charge density is very small away from the interface. We construct numerical solutions corresponding to these configurations, and check that indeed the charge density peaks at the interface. Next, we concentrate on the study of the conductivities of the system. We work in the linear response regime, hence to compute the conductivities we just need study the fluctuations of the worldvolume gauge fields, which couple among themselves and with those of the embedding field. Moreover, for simplicity in this work we do not consider the contribution of a WZ term proposed in [37] as dual to the Quantum Spin Hall effect. This term results from fluctuations of the RR  $C_4$  form of the background. We leave the inclusion of such a term for future work.

The study of the conductivities of our charged holographic interface gives rise to the main results of this work, which we now summarize.

- We compute the AC and DC conductivities both in the direction parallel<sup>1</sup> to the interface ( $\sigma^y$ ) and in the one orthogonal to it ( $\sigma^x$ ). Away from the interface, both conductivities coincide and agree with that of an homogeneous system corresponding to an embedding with constant mass  $m$ . In particular, the resonances corresponding

---

<sup>1</sup>Since the fundamental matter sourced by the D5 lives in a (2+1)-dimensional defect, we consider our system to be (2+1)-dimensional, denoting by  $x$  the direction orthogonal to the (1+1)-dimensional interface and by  $y$  the one parallel to it. Notice that the system is therefore homogeneous along  $y$ .

to the mesonic quasi-particles are clearly visible. At the interface, where the quarks are massless, the conductivity exhibits at low frequency a peak reminiscent of Drude theory. Notice that we are working in the probe approximation, and therefore the charge carriers can relax momentum into the background. Hence, no infinite DC conductivity is to be expected, see [56, 57].

- Due to current conservation,  $\sigma_{\text{DC}}^x$  is independent of  $x$  for a system with a codimension one impurity like ours. Following [58, 59], we can express  $\sigma_{\text{DC}}^x$  purely in terms of horizon data, *i.e.* the behavior of the functions describing the embedding at the black hole horizon. This DC conductivity is basically determined by the system away from the interface, where the charge density is very low.
- The DC conductivity is enhanced along the interface. We observe that  $\sigma_{\text{DC}}^y(x=0)$  is much larger than  $\sigma_{\text{DC}}^x$ . While the latter is determined by the system away from the interface, where the charge density can be very low,  $\sigma_{\text{DC}}^y(x=0)$  is roughly proportional to the value of the charge density at the interface, and is therefore enhanced with respect to  $\sigma_{\text{DC}}^x$ .
- The translational symmetry breaking effects sourced by the interface result in an enhancement of  $\sigma_{\text{DC}}^y$  in its vicinity. Although the system is homogeneous in the  $y$  direction, thanks to the non-linearities of the DBI action, a current along  $y$  is sensitive to the gradients along  $x$  of the embedding fields. We observe a transfer of spectral weight in  $\sigma^y$  from mid to low frequencies, resulting in an enhancement of  $\sigma_{\text{DC}}^y$ .
- We study the competing effects that the presence of the interface has on the DC conductivity in the transverse direction,  $\sigma_{\text{DC}}^x$ . These depend on the relative width of the interface with respect to the total length of the system. When that width is negligible,  $\sigma_{\text{DC}}^x$  is just determined by the homogeneous system away from the interface. On the other hand, when the interface has a sizeable width, it enhances  $\sigma_{\text{DC}}^x$ . Notice that in this case the interface introduces two competing effects: an increase of the charge density on the one hand, and the presence of inhomogeneities along  $x$  on the other. Although, as discussed in [59], these inhomogeneities should suppress the conductivity, we observe that the interface always produces an increase of  $\sigma_{\text{DC}}^x$  with respect to an embedding with constant mass  $m$ .

To summarize, up to well-known effects characteristic of holographic brane intersections, like the constant conductivity in the high frequency limit, or the finite DC conductivity, the behavior of the conductivity observed in our work agrees with broad expectations for a system where charge is localized on a (1+1)-dimensional interface. Moreover, some of the translational symmetry breaking effects sourced by the interface, as the sensitivity of  $\sigma_{\text{DC}}^y$  to the inhomogeneities in the orthogonal direction thanks to the DBI action, are likely to be particular to strongly coupled systems.<sup>2</sup>

This paper is organized as follows. Section 2 is devoted to the construction of the holographic interface. We first introduce the probe-brane embedding of interest and write

---

<sup>2</sup>See [60] for recent results on conductivities in the presence of spatially modulated sources.

down the corresponding action. The embedding is described by two fields, for which we present the IR and UV asymptotic solutions. From the UV solutions we read the values of the chemical potential and the mass, which determine the embedding. We then characterize the part of the phase diagram accessible to the embeddings with finite charge density. In subsection 2.3 we describe the inhomogeneous embeddings that realize a charged interface. Finally, in subsection 2.4 we discuss the numerical methods employed to solve the equations of motion and present examples of numerical solutions corresponding to holographic interfaces. We study the charge density, showing that it peaks at the interface, and analyze how it scales with the chemical potential. Section 3 contains the main results of this work, namely the study of the conductivities for a holographic charged interface. We start by introducing the fluctuations relevant to the computation of the conductivities. We compute the quadratic action for these fluctuations, study the asymptotic solutions of the equations of motion, and discuss the relevant boundary conditions. Subsection 3.2 is focused on the computation of the DC conductivity  $\sigma_{\text{DC}}^x$ , which can be expressed in terms of the horizon data. Next, in subsection 3.3, we explain our numerical methods and boundary conditions, defining two kinds of systems, long and short, for which  $\sigma_{\text{DC}}^x$  exhibits different behaviors. Finally, in subsection 3.4 we present and discuss the results for the conductivity of our setup. We write our conclusions in section 4, where we also discuss some possible directions of future research. We have furthermore included two appendices. Appendix A contains the background equations of motion. In appendix B we write down the quadratic action for the fluctuations relevant for studying the conductivities.

## 2 Localized charge at brane intersections

In this section we consider D3/D5 intersections at nonzero temperature and finite charge density, namely in the presence of a finite density of the fundamental matter dual to the open strings stretching between the D3- and D5-branes. The supersymmetric intersection of  $N$  D3- and  $N_f$  D5-branes along 2+1 spacetime dimensions is dual to (3+1)-dimensional  $\mathcal{N} = 4$  SYM with  $N_f$  fundamental hypermultiplets living on a (2+1)-dimensional defect [45, 46]. We work in the probe limit and at nonzero temperature, hence we treat the D5-branes as probes in the geometry generated by the black D3-branes.

### 2.1 Black D3-branes

According to the AdS/CFT prescription originally proposed in [1],  $\mathcal{N} = 4$  super Yang-Mills theory with an  $SU(N_c)$  gauge group is holographically dual to type IIB string theory on  $AdS_5 \times S^5$  with  $N_c$  units of flux of the Ramond-Ramond five form. The string coupling  $g_s$ , and the coupling of the gauge theory  $g_{\text{YM}}$  are related through  $g_s = g_{\text{YM}}^2/2\pi$ . The AdS curvature radius  $L$  is furthermore related to  $N_c$  and the string tension  $(2\pi\alpha')^{-1}$  by  $L^4/\alpha'^2 = 2g_{\text{YM}}^2 N_c \equiv 2\lambda$ , where  $\lambda$  is the 't Hooft coupling. In the limit of large  $N_c$  and large  $\lambda$  the string side of the duality reduces to weakly coupled classical gravity.

We are interested in finite temperature configurations, and therefore consider the ge-

ometry generated by  $N_c$  black D3-branes, whose metric reads<sup>3</sup> [50]

$$ds^2 = \frac{L^2}{z^2} \left( -\frac{f(z)^2}{h(z)} dt^2 + h(z) d\vec{x}^2 + dz^2 \right) + L^2 d\Omega_5^2, \quad (2.1)$$

where  $\vec{x} = (x_1, x_2, x_3)$ ,  $d\Omega_5^2$  is the metric of a unit radius  $S^5$ , and

$$f(z) = 1 - \frac{z^4}{z_0^4}, \quad h(z) = 1 + \frac{z^4}{z_0^4}. \quad (2.2)$$

This geometry becomes asymptotic to  $AdS_5 \times S^5$  in the small  $z$  limit, with the boundary of  $AdS_5$  being at  $z = 0$ , while it presents a horizon at  $z = z_0$ . Accordingly, the Hawking temperature of the black hole reads

$$T = \frac{\sqrt{2}}{\pi z_0}. \quad (2.3)$$

It is useful to define the dimensionless coordinates

$$(\tilde{z}, \tilde{x}_\mu) = \frac{1}{z_0}(z, x_\mu), \quad (2.4)$$

in terms of which the metric takes the form (2.1) with  $z_0 = 1$ . From now on we always use these dimensionless coordinates and drop the tilde for presentational purposes.

## 2.2 Probe D5-brane

As anticipated, we embed a probe D5-brane in the background generated by the stack of D3-branes (2.1). The embedding is better described by writing the metric of the  $S^5$  in terms of two  $S^2$  as follows

$$d\Omega_5^2 = d\theta^2 + \sin^2 \theta d\Omega_2^2 + \cos^2 \theta d\tilde{\Omega}_2^2. \quad (2.5)$$

We consider the following configuration

	$t$	$x_1$	$x_2$	$x_3$	$z$	$\Omega_2$	$\tilde{\Omega}_2$	$\theta$
D3	$\times$	$\times$	$\times$	$\times$				
D5	$\times$	$\times$	$\times$		$\times$	$\times$		

(2.6)

where the D5-brane shares two Minkowski directions with the D3-branes generating the background, is extended along the radial direction  $z$ , and wraps an  $S^2$  ( $\Omega_2$ ) inside the  $S^5$ , while it is located at a fixed point of the remaining  $S^2$  ( $\tilde{\Omega}_2$ ). The embedding is then described by the coordinate  $\theta$ , which determines the radius of the  $S^2$  wrapped by the D5-brane. In order to simplify the analysis we define

$$\cos \theta = \chi, \quad (2.7)$$

in terms of which we describe the embedding.

---

<sup>3</sup> This metric is related to the more standard Schwarzschild-AdS presentation via the change of coordinates  $z^2 = 2L^4 / (u^2 + \sqrt{u^4 - u_0^4})$ .

We are interested in configurations with finite charge density of the fundamental fields introduced by the flavor D5-brane. Therefore we turn on a nonzero temporal component of the  $U(1)$  worldvolume gauge field

$$A = A_t dt. \quad (2.8)$$

Indeed, its boundary value determines the value of the chemical potential in the dual theory. The embedding of the probe D5-brane is then determined by the two fields  $\chi$  and  $A_t$ .

### 2.2.1 Action and equations of motion

In order to describe setups where the embedding of the D5-brane depends on one of the spatial directions, we let the fields  $\chi$  and  $A_t$  depend on the radial variable  $z$ , and on one of the Minkowski directions;  $x_1$  (just  $x$  in the following).<sup>4</sup> Hence the embedding is characterized by  $\chi(z, x)$  and  $A_t(z, x)$ .

The dynamics of the system is governed, in the probe approximation, by the DBI action for the D5-brane in the background sourced by the black D3-branes

$$S = -N_f T_{D5} \int d^6x \sqrt{-\det(P[g] + 2\pi \alpha' F)}, \quad (2.9)$$

where  $P[g]$  is the pullback of the metric on the worldvolume of the D5-brane and  $F$  the field strength of the worldvolume  $U(1)$  gauge field. For our setup the DBI action can be written as<sup>5</sup>

$$S = -N_f T_{D5} L^6 \int dt d^2x dz d\Omega_2 f z^{-4} \sqrt{h(1 - \chi^2)(S_\chi + S_\phi + S_{\text{int}})}, \quad (2.10)$$

with

$$S_\chi = 1 - \chi^2 + z^2 \chi'^2 + \frac{z^2 \dot{\chi}^2}{h}, \quad (2.11)$$

$$S_\phi = -\frac{z^4(1 - \chi^2)}{f^2} (h \phi'^2 + \dot{\phi}^2), \quad (2.12)$$

$$S_{\text{int}} = -\frac{z^6(\dot{\chi}\phi' - \chi'\dot{\phi})^2}{f^2}, \quad (2.13)$$

where a tilde denotes a derivative with respect to  $z$  and a dot a derivative with respect to  $x$ . Moreover,  $\phi$  stands for the dimensionless temporal component of the gauge field defined via

$$\phi = 2\pi\alpha' \frac{z_0}{L^2} A_t. \quad (2.14)$$

The equations of motion for  $\phi(z, x)$  and  $\chi(z, x)$  can be readily obtained from the action (2.10). The resulting lengthy expressions are shown in appendix A. In the following we analyze their IR ( $z \rightarrow 1$ ) and UV ( $z \rightarrow 0$ ) asymptotic solutions.

<sup>4</sup>As far as the dependence on  $x_2$  and  $x_3$  is concerned, it is consistent to locate the D5-brane at  $x_3 = 0$ , and consider embeddings homogeneous along  $x_2$ , which we call  $y$  in the following.

<sup>5</sup>It is straightforward to check that for the embedding at hand there is no contribution to the action coming from the WZ term.



## IR Asymptotics

As we explain below, we are interested in solutions describing black hole embeddings for which the brane ends at the horizon. Hence regularity at the horizon requires  $\phi$  and  $\chi'$  to vanish there, restricting the IR solution to the following form

$$\phi(z, x) = a^{(2)}(x) (1 - z)^2 + \mathcal{O}((1 - z)^3), \quad (2.15a)$$

$$\chi(z, x) = C^{(0)}(x) + C^{(2)}(x) (1 - z)^2 + \mathcal{O}((1 - z)^3), \quad (2.15b)$$

with

$$C^{(2)}(x) = \frac{(2 - a^{(2)}(x)^2) \left[ C^{(0)''}(x) (C^{(0)}(x)^2 - 1) - C^{(0)}(x) (3C^{(0)'}(x)^2 + 4) + 4C^{(0)}(x)^3 \right]}{8 [C^{(0)'}(x)^2 - 2C^{(0)}(x)^2 + 2]}. \quad (2.16)$$

## UV Asymptotics

At the boundary, the asymptotic form of the fields  $\chi(z, x)$  and  $A(z, x)$  can be found to be of the form

$$\phi(z, x) = \mu(x) - \rho(x)z + \mathcal{O}(z^2), \quad (2.17a)$$

$$\chi(z, x) = m(x)z + \psi(x)z^2 + \mathcal{O}(z^3). \quad (2.17b)$$

Let us recall that the holographic dictionary relates  $\mu(x)$ , and  $\rho(x)$  respectively to the chemical potential and charge density of the  $U(1)$  flavor symmetry supported by the D5-brane. As for the asymptotic form of  $\chi$ , the leading piece  $m(x)$  is proportional to the asymptotic distance  $\bar{M}$  between the probe D5 and the D3-branes generating the background, and is therefore interpreted as the quark mass. The subleading contribution  $\psi(x)$  is associated to the vacuum expectation value of the bilinear quark-antiquark operator sourced by the flavor D5-brane, namely the quark condensate. In order to make these identifications more precise, let us bring the dimensions back into the game. First, we recall that the dimensionful chemical potential  $\bar{\mu}$  and charge density  $\bar{\rho}$  are read from the asymptotic form of the temporal component of the gauge field as

$$A_t = \bar{\mu}(x) - \bar{\rho}(x)z + \dots \quad (2.18)$$

Hence, recalling the redefinitions (2.4) and (2.14), the temperature of the black hole (2.3), and using that  $\sqrt{\lambda} = L^2/(\sqrt{2}\alpha')$  we arrive at

$$\mu = \frac{2}{\sqrt{\lambda}} \frac{\bar{\mu}}{T}, \quad \rho = \frac{2\sqrt{2}}{\pi\sqrt{\lambda}} \frac{\bar{\rho}}{T^2}. \quad (2.19)$$

As for the quark mass, we follow [50] and define  $M_q = \sqrt{\lambda} \bar{M}/2$ , where  $\bar{M} = m/z_0$ . This allows us to write

$$m = \frac{2\sqrt{2}}{\pi\sqrt{\lambda}} \frac{M_q}{T}. \quad (2.20)$$

As is clear from (2.17), the UV solutions depend on four parameters (functions of  $x$ ):  $\mu$ ,  $\rho$ ,  $m$ , and  $\psi$ , while as we see in (2.15), the IR behavior is determined by two free functions,

namely  $C^{(0)}(x)$  and  $a^{(2)}(x)$ . Thus we expect a two-parameter family of solutions, which we choose to describe in terms of the chemical potential  $\mu$ , which we choose to be independent of  $x$ , and the mass  $m(x)$ . Consequently, once  $\mu$  and  $m(x)$  are fixed, the embedding of the probe D5-brane is completely fixed.

### 2.3 Inhomogeneous embeddings and charge localization

The phenomenology of Dp/Dq brane intersections, both at zero and finite temperature, with and without charge density, has been thoroughly studied over the last ten years, see for instance [61–63] and references therein.

We now review some features that are relevant for our construction. Embeddings of the probe D5-brane in the black D3-brane background generally fall into two qualitatively different categories labeled Minkowski and black hole (BH). Minkowski embeddings are those in which the D5-brane never reaches the black hole, while for the BH embeddings the probe brane ends at the horizon. Minkowski embeddings exist above a certain value of the mass, while BH embeddings are possible for any mass. A phase transition between these two embeddings occurs as the ratio  $M_q/T$  is varied; this is known as meson melting [50] since stable mesonic states exist for Minkowski embeddings, but not for black hole ones. This phase transition also happens in the presence of a chemical potential, and the corresponding phase diagram has been studied in [51] (see also [54]).

A feature that is crucial for our construction stems from the fact that at nonzero charge density only BH embeddings are possible. As explained in [53], the fundamental strings realizing the charge density would have nowhere to end in a Minkowski embedding. Moreover, as illustrated in figure 1, for a large enough  $M_q/T$ , BH embeddings exist only above a nonzero chemical potential  $\bar{\mu}/T$ . In particular, the shaded region in the plot is only accessible by Minkowski embeddings, which have zero charge density. Since it will be useful later, in figure 2 we plot the same data as in fig. 1, but now for  $\bar{\mu}/M_q$  versus  $T/M_q$ . In terms of these variables the forbidden region corresponds to the triangular region visible at  $T/M_q \lesssim 0.6$ .

As explained above, our purpose is to construct an embedding depending on one spatial direction  $x$ , that localizes charge density along an interface situated at  $x = 0$ . This can be done, following [36], by means of an embedding with constant chemical potential  $\mu = \bar{\mu}/T$ , and an  $x$ -dependent mass ( $m = M_q/T$ )

$$m(x) = M \left( \frac{2}{1 + e^{-ax}} - 1 \right), \quad (2.21)$$

that interpolates between two constant values;  $M$  at  $x \rightarrow -\infty$ , and  $-M$  at  $x \rightarrow \infty$ , while vanishing at the origin,  $m(0) = 0$ .<sup>6</sup> Notice that  $a$  is a constant parameter that fixes the steepness of the kink. Ideally, if we chose  $\mu$  and  $M$  to lie in the shaded region of figure 1, asymptotically, at  $x \rightarrow \pm\infty$ , the embedding should be of the Minkowski type, and therefore the charge density would vanish. At the interface ( $x = 0$ ) though, the mass vanishes, the

---

<sup>6</sup>As explained in [37], embeddings with positive and negative  $m$  correspond respectively to the D5-brane sitting at opposite poles of the  $\tilde{\Omega}_2$  in (2.6). As in [36] we account for the case  $m < 0$  by letting  $\chi$  become negative.

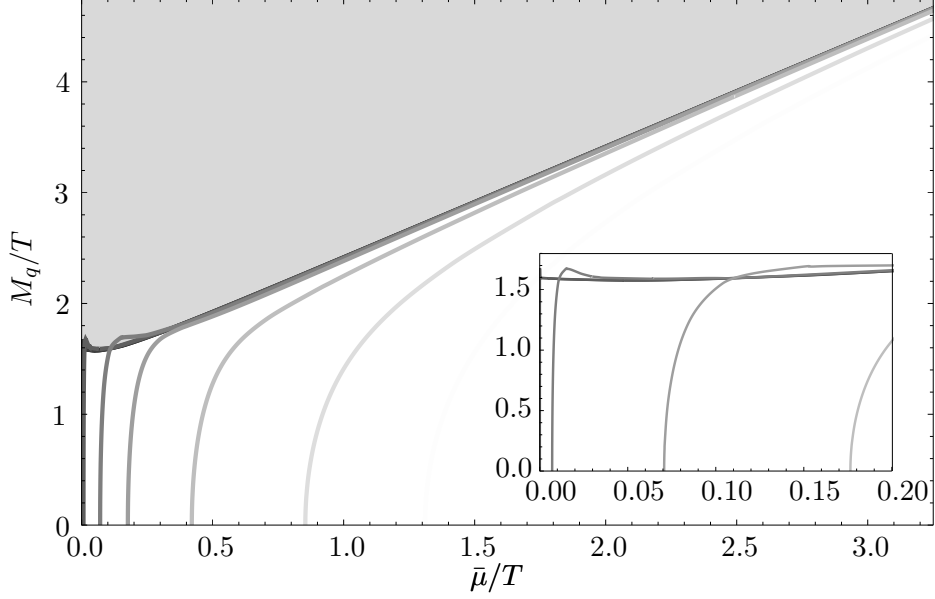


**Figure 1:** Quark mass  $m = M_q/T$  versus chemical potential  $\mu = \bar{\mu}/T$  for black hole embeddings corresponding to various values of the charge density  $\rho = \bar{\rho}/T^2$ , decreasing from right to left:  $\rho = 2, 1.25, 0.6, 0.25, 0.1, 0.01, 10^{-4}, 10^{-6}$ . The shaded area is not accessible by BH embeddings, and is asymptotically delimited (at large  $\mu$ ) by  $m > 1.00\mu + 1.41$ . In the inlay we zoom in on the region of low  $\mu$ .

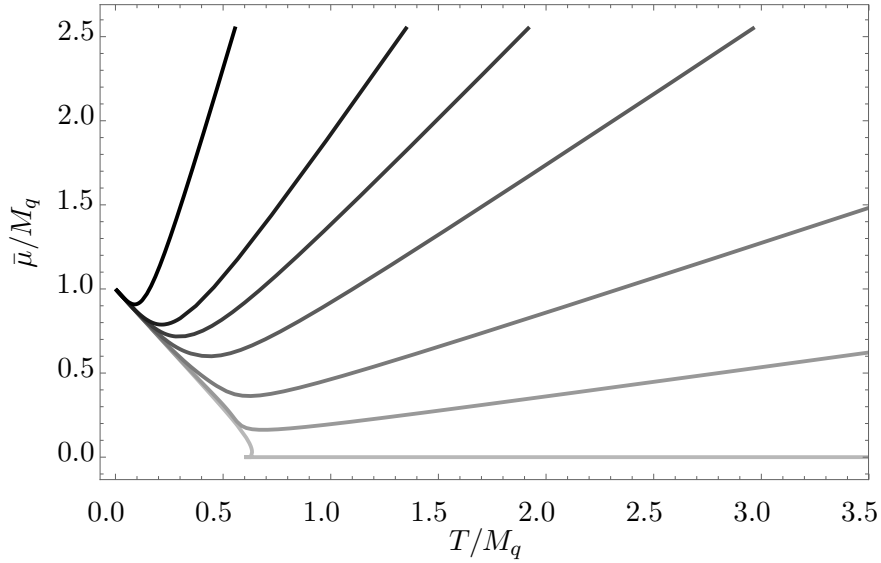


**Figure 2:** As in fig. 1 we plot lines of constant charge density for BH embeddings. From bottom (light gray) to top (black) they correspond to  $\rho = 10^{-6}, 0.25, 0.6, 1.25, 2, 3, 10$ .

brane must intersect the BH, and, for a nonzero  $\mu$ , some charge density is induced. In such a construction the charge density would exactly vanish towards the spatial edges, while it would peak at the interface. Notice that by increasing  $a$  in (2.21) the transition can be

made as abrupt as desired, and therefore the charge may be localized at  $x \sim 0$ . However, such an embedding, with a varying topology along  $x$ , turns out to be too challenging in numerical terms. Instead, we do as in [41], and settle for a more modest construction: we choose  $M$  and  $\mu$  to be just outside, but at the edge of, the shaded region of figure 1. So we deal with embeddings that are of the BH kind everywhere. Notice that in principle one can pick  $M$  and  $\mu$  such that the corresponding embedding has an arbitrarily small charge density induced at the edges. Then, effectively the charge density is localized around the interface, where the embedding becomes massless.

## 2.4 Numerical Results

In this section we present numerical solutions realizing the inhomogeneous embeddings described in the previous section. In order to construct those embeddings we must solve the equations of motion for the fields  $\chi(z, x)$  and  $\phi(z, x)$ , and the inhomogeneous mass profile boundary condition (2.21) implies that we have to deal with two coupled second order PDEs which we solve numerically.

Before describing our numerical method, let us recall the boundary conditions to be imposed on the two equations of motion. First, in the UV ( $z = 0$ ), from (2.17) and (2.21), we impose

$$\chi'(0, x) = M \left( \frac{2}{1 + e^{-ax}} - 1 \right), \quad \phi(0, x) = \mu, \quad (2.22)$$

where  $\mu$  determines the homogeneous chemical potential of the solution, while  $M$  fixes the mass of the embedding at the edges of the system. On the other hand, at the horizon ( $z = 1$ ) the asymptotic solutions (2.15) result in the following boundary conditions

$$\phi(1, x) = 0, \quad \chi'(1, x) = 0. \quad (2.23)$$

As for the boundary conditions at the spatial edges, note that the symmetry of our setup does not allow the use of periodic boundary conditions. We take our system to have a finite length ( $x \in [-L, L]$ ), but require it to be large enough so that it resembles an homogeneous embedding towards the spatial edges. Consequently we impose the following Neumann boundary conditions

$$\dot{\chi}(z, \pm L) = 0, \quad \dot{\phi}(z, \pm L) = 0, \quad (2.24)$$

which ensure that the effects of the inhomogeneity sourced by the mass profile (2.21) fade away towards the edges.

Regarding the numerics, we resort to pseudospectral methods implemented in Mathematica, discretizing the plane  $(z, x)$  on a grid of Chebyshev points, and then solving the resulting set of nonlinear algebraic equations via Newton-Raphson iteration. Defining the variations of the fields  $f = (\chi, \phi)$  in each iteration by  $\delta f$ , we consider the accuracy of our solution to be given by  $\text{Max } |\delta f|$ .

In addition, we can benefit from the symmetry of our setup by noting that  $\chi(z, x)$  is an odd function of  $x$ , whereas  $\phi(z, x)$  is even

$$\chi(z, x) = -\chi(z, -x), \quad \phi(z, x) = \phi(z, -x). \quad (2.25)$$

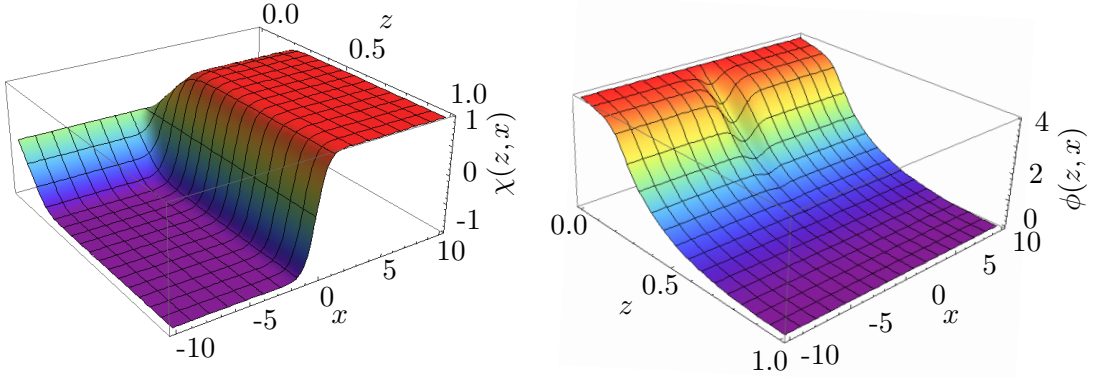


**Figure 3:** Computed solutions of  $\chi(z, x)$  and  $A(z, x)$  for  $\mu = 4$  and  $M = 5.34$ .

This follows from the form of the equations of motion together with our UV boundary conditions (2.22), and helps us making the numerics more efficient in two ways. First, it allows us to solve for half the range along  $x$ , imposing (2.24) at  $x = L$ , while in view of 2.25 at  $x = 0$  we must have

$$\chi(z, 0) = 0, \quad \dot{\phi}(z, 0) = 0. \quad (2.26)$$

Second, given that Chebyshev collocation points are more densely concentrated towards the boundaries of the interval, this reduction of the integration range results in a better accuracy of our solutions around the interface (at  $x = 0$ ), where the gradients along  $x$  are larger.

Having described the numerical method we employ to construct the embeddings, we now present the output of the numerical computation. We have used a grid of  $50 \times 50$  collocation points for the half-interval of integration ranging from  $x = 0$  to  $x = 10$ .

According to what we have discussed in section 2.3 we have chosen the values of  $M$  and  $\mu$  to be such that the charge density induced at the edges of our system is much lower than that at the interface. In figure 3 we plot the numeric solution for the fields  $\chi(z, x)$  and  $\phi(z, x)$ , for a case where  $\mu = 4$  and  $M = 5.34$ . The parameter  $a$  is chosen so that the numerics remain stable while still having a steep embedding.  $a = 3$  turns out to be good enough for this<sup>7</sup>. It is worth mentioning how the spatial inhomogeneity introduced by the step-like boundary condition (2.21) affects differently the two fields defining our setup. While for  $\chi$  the inhomogeneity is amplified towards the horizon, for the gauge field  $\phi$  it dies away towards the horizon.

In figure 4 we present the resulting charge density, which through (2.17a) is given by the radial derivative of  $\phi$  evaluated at the boundary. Indeed, we see that the charge density peaks at the interface, where its value is about five times the value at the edges.

Finally, it is interesting to study how the charge density depends on the chemical potential, both at the interface and far from it. This is plotted in figure 5, where we

<sup>7</sup>While the numerics allow for much larger values of  $a$  for the computation of the background, these pose some difficulties when it comes to solving for the perturbation fields.

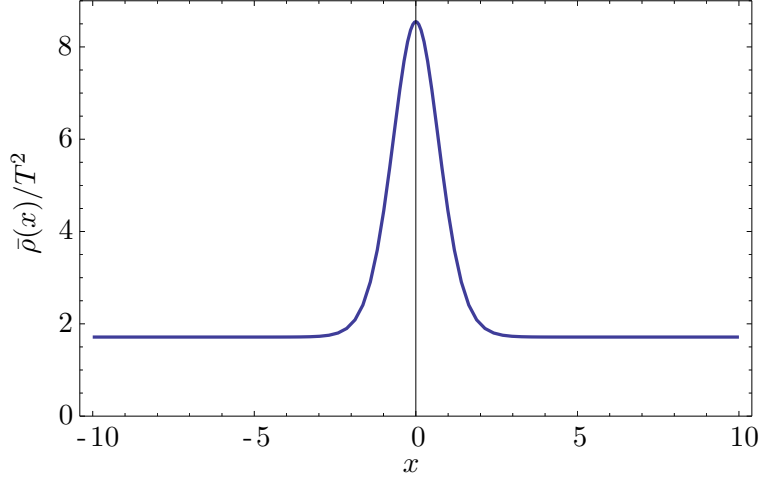


**Figure 4:** Charge density  $\rho(x) = \bar{\rho}(x)/T^2$  for the background in figure 3. The base line is at  $\rho = 1.71$ , and the peak reaches  $\rho = 8.54$ .

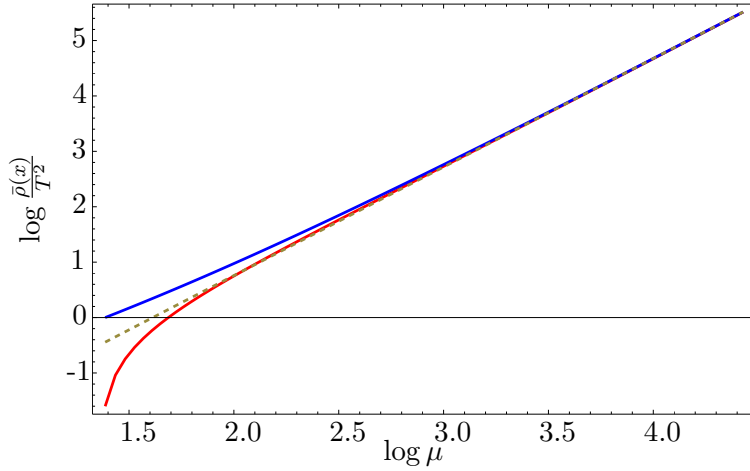


**Figure 5:** Charge density  $\rho(x)$  versus chemical potential  $\mu$  for an embedding with  $M = 5.3$ . The blue line corresponds to the interface, while the red one to one of the spatial edges. The charge density has been normalized to unity at  $\mu = 1$ ,  $m = 0$ . The dashed line illustrates the fit  $\rho = \mu^{1.96}$  performed for  $\mu > 74$ .

observe that the scaling  $\rho \propto \mu^2$  expected for a D3/D5 intersection [64] is approached everywhere in our system for large enough  $\mu$ .

### 3 Conductivities

After constructing a holographic setup localizing charge along a (1+1)-dimensional defect, we go on to study its response to an applied electric field. In the rest of this work we study the AC and DC conductivities of our system both in the direction parallel,  $y$ , and orthogonal to the defect,  $x$ . In order to do so, we compute the linear response of our background when an electric field is switched on along the boundary. We must then study the fluctuations of the worldvolume gauge field along the Minkowski directions. In general

these are coupled among them and to the fluctuations of the embedding field  $\chi$ , thus we have to solve for the whole set of coupled fields.

### 3.1 Fluctuations

We are interested in switching on fluctuations of the gauge field realizing an electric field of constant modulus and frequency  $\omega$  along the boundary, hence at  $z = 0$  those fluctuations must satisfy

$$f_{ti} = (i\omega \epsilon_i) e^{i\omega t}, \quad (i = x, y). \quad (3.1)$$

where  $f_{ti}$  stands for the field strength of the fluctuations of the gauge field, and we are considering both the case when the electric field is orthogonal to the interface (with constant modulus  $\epsilon_x$ ), and parallel to it ( $\epsilon_y$ ). Consequently, we must study the following set of fluctuations<sup>8</sup>

$$A_\mu = A_\mu(z, x) + a_\mu(z, x) e^{i\omega t}, \quad (3.2a)$$

$$\chi = \chi(z, x) + c(z, x) e^{i\omega t}, \quad (3.2b)$$

where the uppercase  $A_\mu$  and  $\chi$  stand for the background fields, while lowercase  $a_\mu$  and  $c$  refer to the fluctuations of the gauge field and the embedding scalar respectively<sup>9</sup>. Our background, described by  $A_t(z, x)$  and  $\chi(z, x)$ , is both time invariant and translation invariant along the  $y$  direction. This allows us to Fourier transform both along  $t$  and  $y$ , and since we are interested only in the conductivity we consider our fluctuations to have no net spatial momentum. In addition, we choose to work in the radial gauge and therefore set

$$a_z(z, x) = 0. \quad (3.3)$$

We are working in the linear response regime, hence the equations of motion for the fluctuations (3.2) follow from expanding the DBI action (2.9) up to second order in those fluctuations. The resulting quadratic action  $S^{(2)}$  is shown in appendix B. Although straightforward to derive, the resulting equations of motion are lengthy and we do not reproduce them here. However, it is worth mentioning that the component of the gauge field fluctuations parallel to the defect,  $a_y$ , decouples from the rest of the fluctuations. Hence to study the conductivity  $\sigma_y$  we only need to solve the corresponding linear partial differential equation (PDE) for  $a_y$ . Instead,  $a_x$  is coupled to both  $a_t$ , and  $c$ . Their dynamics is described by a system of three second order linear PDEs plus a first order constraint PDE resulting from the equation of motion for  $a_z$ .

The conductivity is given by the retarded correlator of the worldvolume  $U(1)$  current. In order to compute it, we must solve the equations of motion of the fluctuations with

---

<sup>8</sup>We are working with the dimensionless coordinates (2.4), hence  $\omega$  is dimensionless, and in terms of the dimensionful frequency  $\mathfrak{w}$ , one has  $\omega = \sqrt{2} \mathfrak{w} / (\pi T)$ .

<sup>9</sup>We need apply the same field redefinition as in (2.14) to the fluctuations of the gauge field. However, for notational simplicity we do not introduce a new label and just assume that we have rescaled the fields as  $a_\mu \rightarrow L^2 / (2\pi\alpha' z_0) a_\mu$ .

infalling boundary conditions at the horizon. Then we can read the electric current on the boundary,  $j_i$ , and therefore compute the conductivity as<sup>10</sup>

$$\sigma_i(\omega, x) = \frac{j_i}{i\omega \mathbf{e}_i} = \lim_{z \rightarrow 0} \frac{f_{iz}}{f_{ti}}, \quad (i = x, y). \quad (3.4)$$

We now study the asymptotic behavior of the fluctuations both in the IR and UV. This allows us to properly choose the boundary conditions when solving the corresponding equations of motion. It is easy to check that the fields behave in the UV ( $z \rightarrow 0$ ) as

$$a_\mu(z, x) = a_\mu^{(b)}(x) - j_\mu(x) z + \mathcal{O}(z^2), \quad (\mu = t, x, y), \quad (3.5a)$$

$$c(z, x) = c^{(b)}(x) z + \mathcal{O}(z^2), \quad (3.5b)$$

while in the IR ( $z \rightarrow 1$ ) they take the form

$$a_\mu = (1 - z)^{i\alpha_\pm} \left( a_\mu^{(0)}(x) + a_\mu^{(1)}(x) (1 - z) + \mathcal{O}((1 - z)^2) \right), \quad (3.6a)$$

$$c = (1 - z)^{i\alpha_\pm} \left( c^{(0)}(x) + c^{(1)}(x) (1 - z) + \mathcal{O}((1 - z)^2) \right), \quad (3.6b)$$

with

$$\alpha_\pm = \pm \frac{\omega}{2\sqrt{2}}. \quad (3.7)$$

Notice that with our conventions (see (3.2)) it is the positive root  $\alpha_+$  the one corresponding to an infalling solution at the horizon. For this choice we obtain the following solution for the first order ( $x$ -dependent) coefficients

$$c^{(1)} = \frac{i\omega}{4\sqrt{2}} c^{(0)}, \quad a_t^{(0)} = 0, \quad a_i^{(1)} = \frac{i\omega}{4\sqrt{2}} a_i^{(0)}; \quad (i = x, y), \quad (3.8)$$

while higher order coefficients are determined in terms of these.

We now have all ingredients needed to compute the conductivity by solving the equations of motion of the fluctuations. First, as is clear from the form of the IR solutions (3.6), it is useful to redefine the fields as

$$\tilde{a}_\mu(z, x) = (1 - z)^{-i\alpha_+} a_\mu(z, x), \quad \tilde{c}(z, x) = (1 - z)^{-i\alpha_+} c(z, x). \quad (3.9)$$

Then, at the horizon we impose the following mixed Dirichlet and Robin boundary conditions

$$\tilde{a}_t(1, x) = 0, \quad \tilde{a}'_i(1, x) = \frac{i\omega}{4\sqrt{2}} \tilde{a}_i(1, x), \quad \tilde{c}'(1, x) = \frac{i\omega}{4\sqrt{2}} \tilde{c}(1, x). \quad (3.10)$$

At the boundary we want our fluctuations to source an homogeneous electric field (3.1). When computing the conductivity parallel to the defect (we need only solve for  $a_y$ ), we impose

$$a_y(0, x) = 1, \quad (3.11)$$

---

<sup>10</sup>Here and in the following we are rescaling the conductivity by the dimensionless constant appearing in front of the action (2.10), *i.e.*  $\sigma \rightarrow \sigma/(N_f T_{D5} L^6)$ , so that we recover the usual high frequency CFT result  $\lim_{\omega \rightarrow \infty} \sigma = 1$ .



where we are normalizing the modulus of the electric field to unity ( $\epsilon_y = 1$ ). Instead, to compute  $\sigma_x$  we must solve for  $a_x$ ,  $a_t$ , and  $c$ . Again, we want our fluctuations to source solely an electric field in the  $x$  direction. Hence

$$c'(0, x) = 0, \quad (3.12a)$$

$$a_x(0, x) - \frac{1}{i\omega} \partial_x a_t(0, x) = 1, \quad (3.12b)$$

where the first condition ensures that no fluctuations of the mass are sourced, whereas the second implies that an homogeneous electric field along  $x$ , normalized to  $\epsilon_x = 1$ , is turned on at the boundary. In addition, in the UV we impose the fulfillment of the constraint equation, which reduces to

$$i\omega \partial_z a_t(0, x) - \partial_x \partial_z a_x(0, x) = 0. \quad (3.13)$$

Notice that in terms of the asymptotic solutions (3.5a) this boundary condition is nothing else than the conservation of current

$$\partial_t (e^{i\omega t} j_t(x)) - e^{i\omega t} \partial_x j_x(x) = 0. \quad (3.14)$$

As expected, it is straightforward to check that the partial derivative along  $z$  of the constraint equation vanishes for solutions of the equations of motion. This ensures that the constraint is satisfied for all  $z$  by any solution of the equations of motion that obeys the constraint on a constant  $z$  slice.

Finally, one should notice that although we have allowed for both  $a_t$  and  $a_x$  to be nonzero at the boundary, one can proceed as in [12, 18] and apply a gauge transformation  $e^{i\omega t} \Lambda(z, x)$  that brings the boundary field configuration to

$$a_\mu(0, x) e^{i\omega t} dx^\mu \rightarrow (a_\mu + \partial_\mu \Lambda(0, x)) e^{i\omega t} dx^\mu = e^{i\omega t} dx, \quad (3.15)$$

which makes clear that the only boundary source is that corresponding to an homogeneous electric field, and other nonzero sources are just gauge artifacts.<sup>11</sup>

Summing up, in order to compute the conductivity  $\sigma_y(\omega)$  we must solve the equation of motion of  $a_y$  with boundary conditions (3.10) and (3.11), and then read the conductivity from (3.4). On the other hand, to calculate  $\sigma_x$  we need solve the equations of motion of  $a_x$ ,  $a_t$ , and  $c$ , imposing (3.10) at the horizon, and (3.12 - 3.13) on the boundary; and again read  $\sigma_x(\omega)$  from (3.4). We will discuss the boundary conditions at the spatial boundaries when describing our numerical methods. But before that, in the next section we analyze the DC limit of the conductivity, and show how  $\sigma_x^{\text{DC}}$  can be computed from the background horizon data, with no need to solve for the fluctuations.

### 3.2 DC conductivity

We can follow the procedure of [58] (as applied for instance in [59] to a DBI action) and compute the DC conductivity along the direction perpendicular to the interface  $\sigma_x^{\text{DC}}$  in terms of the background functions evaluated at the horizon.

---

<sup>11</sup>Notice that one can always choose  $\Lambda(z, x)$  such that it vanishes at the horizon (so  $a_t$  is still zero there), and also satisfies  $\partial_z \Lambda(0, x) = 0$  (and hence  $a_z(0, x) = 0$ ).

Let us start by defining the radial coordinate  $\zeta$  through

$$d\zeta = \sqrt{\frac{h(z)}{f(z)^2}} dz, \quad (3.16)$$

and note that the horizon (at  $z = 1$ ) is located at  $\zeta = \infty$  in the new coordinate. When expressed in this coordinate, the equations of motion for the fluctuation fields  $a_x(z, x)$  and  $a_z(z, x)$  in the DC limit,  $\omega \rightarrow 0$ , respectively take the form

$$\partial_\zeta (\mathcal{F}(\zeta, x) \partial_\zeta a_x) = 0, \quad \partial_x (\mathcal{F}(\zeta, x) \partial_\zeta a_x) = 0, \quad (3.17)$$

where we have defined

$$\mathcal{F}(z, x) = f (1 - \chi^2)^{3/2} \sqrt{\frac{h}{\Gamma}}, \quad (3.18)$$

with

$$\begin{aligned} \Gamma = & -z^4 h \left\{ \phi'^2 [h(1 - \chi^2) + z^2 \dot{\chi}^2] - 2z^2 \phi' \dot{\phi} \chi' \dot{\chi} + \dot{\phi}^2 (1 - \chi^2 + z^2 \chi'^2) \right\} \\ & - f^2 [h (\chi^2 - 1 - z^2 \chi'^2) - z^2 \dot{\chi}^2]. \end{aligned} \quad (3.19)$$

The equations of motion (3.17) ensure that the combination  $\mathcal{F} \partial_\zeta a_x$  is a constant. It is thanks to the existence of this conserved quantity that one can express  $\sigma_x^{\text{DC}}$  in terms of the background functions evaluated at the horizon. First, notice that at the boundary

$$\mathcal{F}(0, x) = 1, \quad (3.20)$$

and let us define the function

$$X(\zeta, x) = -\frac{\partial_\zeta a_x(\zeta, x)}{a_x(\zeta, x)}, \quad (3.21)$$

which at the horizon satisfies

$$X(\infty, x) = i\omega, \quad (3.22)$$

due to the ingoing wave boundary condition imposed on  $a_x$ . In terms of  $X(\zeta, x)$ , the conductivity from (3.4) reads

$$\sigma_x(\omega, x) = \frac{X(0, x)}{i\omega} a_x(0, x), \quad (3.23)$$

where we have normalized the modulus of the electric field to one. Next, in the DC limit we can expand  $X$  in a power series in  $\omega$  as

$$X(\zeta, x) = i\omega a(\zeta, x) + \mathcal{O}(\omega^2), \quad (3.24)$$

and  $a_x$  and  $a_t$  at the boundary as

$$a_t(0, x) = i\omega p(x) + \mathcal{O}(\omega^2), \quad (3.25a)$$

$$a_x(0, x) = 1 + \partial_x p(x) + \mathcal{O}(\omega), \quad (3.25b)$$

where  $a(\zeta, x)$  and  $p(x)$  are fixed by the equations of motion (3.17). Moreover, notice that (3.25) is such that the condition (3.1) of having a constant electric field (with  $\mathfrak{e}_x = 1$ ) at the boundary is automatically satisfied. At the horizon, the ingoing wave condition (3.22) translates into

$$a(\infty, x) = 1. \quad (3.26)$$

Plugging the expansions (3.24, 3.25) into eq. (3.23) we obtain

$$\sigma_x^{\text{DC}} = a(0, x)(1 + \partial_x p(x)). \quad (3.27)$$

Using the definition (3.21) together with the expansions (3.24, 3.25), the equations of motion (3.17) imply that

$$\mathcal{F}(\zeta, x) a(\zeta, x) (1 + \partial_x p(x)) \quad (3.28)$$

is a constant<sup>12</sup>. Now, notice that (3.28) when evaluated at  $\zeta = 0$  reduces precisely to the expression (3.27) for the conductivity. Hence we conclude that  $\sigma_x^{\text{DC}}$  is a constant. By evaluating (3.28) at the horizon we arrive at the following expression for the DC conductivity

$$\sigma_x^{\text{DC}} = \mathcal{F}(z = 1, x) (1 + \partial_x p(x)), \quad (3.29)$$

which is indeed a constant as required by current conservation. Notice though, that this expression for  $\sigma_x^{\text{DC}}$  still depends on the fluctuations through the field  $p(x)$  which should in principle be determined by solving the corresponding equations of motion. However, this dependence can be eliminated and  $\sigma_x^{\text{DC}}$  expressed solely in terms of the background horizon data. Integrating the expression (3.29) over the whole sample we can write

$$\sigma_x^{\text{DC}} \frac{1}{2L} \int_{-L}^L \frac{dx}{\mathcal{F}(1, x)} = \frac{1}{2L} \int_{-L}^L dx (1 + \partial_x p(x)), \quad (3.30)$$

and assuming the condition

$$\frac{1}{2L} \int_{-L}^L dx (1 + \partial_x p(x)) = 1, \quad (3.31)$$

(to be justified below) we arrive at the following expression for the DC conductivity

$$\sigma_x^{\text{DC}} = \frac{2L}{\int_{-L}^L \frac{dx}{\mathcal{F}(1, x)}}, \quad (3.32)$$

which allows us to calculate  $\sigma_x^{\text{DC}}$  purely in terms of background functions evaluated at the horizon. In terms of the IR asymptotic solutions for  $\phi$  and  $\chi$ , given in eq. (2.15),  $\mathcal{F}(z = 1, x)$  can be written as

$$\mathcal{F}(z = 1, x) = \frac{2 \left( C^{(0)}(x)^2 - 1 \right)^{3/2}}{\sqrt{(a^{(2)}(x)^2 - 2) \left( 2 - 2C^{(0)}(x)^2 + C^{(0)'}(x)^2 \right)}}. \quad (3.33)$$

---

<sup>12</sup>We have taken into account that  $a_x(\zeta, x) = a_x(0, x) + \mathcal{O}(\omega)$ .

To end this section, let us discuss the condition (3.31) that must be satisfied by the fluctuations. First, notice that when rewritten in terms of  $a_t(z, x)$  it boils down to

$$\int_{-L}^L dx \partial_x a_t(0, x) = 0. \quad (3.34)$$

This would be automatically satisfied for a periodic system, but also in a setup like ours if we assume that the system is long enough for the effects of the interface to fade away towards the edges of the sample. As we discuss below, it can be checked that in that case the solution for the fluctuations asymptotes towards the edges to that of a homogeneous system, for which  $a_t = 0$  and then (3.34) holds. A more general argument for requiring (3.34) to hold is as follows. Notice that even though we allow  $a_t$  to be nonzero at the boundary, as illustrated by (3.15) our configuration is gauge equivalent to one where  $a_x$  is the only source at the boundary [12, 18]. Then,  $a_t(0, x)$  is pure gauge, *i.e.*  $\Lambda(0, x)$ , and gauge invariance of the action in presence of a conserved current implies that  $\int_{-L}^L dx \partial_x \Lambda(0, x) = 0$ , which justifies the assumption (3.34).

### 3.3 Numerics

As discussed above, in order to compute the conductivity, we solve the equations of motion of the fluctuations numerically. We now briefly describe the numerical methods employed, and specify the boundary conditions imposed at the spatial edges of the system.

We solve the equations of motion of the fluctuation fields (3.9) on the same Chebyshev grid used for the background. To simplify the numerics, we make use of the parity along  $x$  of the fields in our problem, namely

$$\begin{aligned} a_t(z, x) &= -a_t(z, -x), & a_x(z, x) &= a_x(z, -x), \\ c(z, x) &= c(z, -x), & a_y(z, x) &= a_y(z, -x), \end{aligned} \quad (3.35)$$

which follows straightforwardly from the (linear) equations of motion taking into account that the background fields satisfy (2.25). As in the case of the background, this allows us to actually solve for half the system, between  $x = -L$  and  $x = 0$ , and given the distribution of points in a Chebyshev grid, greatly increases the resolution close to the interface, where the gradients in  $x$  are larger. The IR and UV boundary conditions are given by eqs. (3.8, and 3.11 - 3.13) as discussed above.

Regarding the boundary conditions at the spatial edges ( $x = \pm L$ ), again, periodic boundary conditions cannot be used due to the symmetry of the problem. Let us focus first on the three coupled fields  $a_t$ ,  $a_x$ , and  $c$ , which allow us to compute  $\sigma_x$ . By studying the asymptotic form of the coupled PDEs at the spatial boundaries, one can show that a solution is completely determined once the values of  $a_t$  and  $c$ , or those of their derivatives  $\partial_x a_t$  and  $\partial_x c$ , are fixed at each spatial boundary<sup>13</sup>. The case of  $a_y$  is simpler, for we just

---

<sup>13</sup>Solving the system asymptotically at one edge, once the values of  $a_t$  and  $c$ , and their derivatives  $\partial_x a_t$  and  $\partial_x c$ , are fixed, the asymptotic solution for  $a_x$ ,  $a_t$  and  $c$  is fully determined (one needs plug in the UV and IR boundary conditions too). Then, to fully determine a solution of the system one can fix the values of  $a_t$  and  $c$ , and their derivatives, at one edge, or equivalently impose two conditions at one edge and two more at the other. We consider fixing  $a_t$  and  $c$  both at  $x = L$  and  $x = -L$ , or, alternatively, fixing  $\partial_x a_t$  and  $\partial_x c$  at  $x = \pm L$ .

need to solve a linear PDE, and as spatial boundary conditions we either fix the value of the function, or of its derivative  $\partial_x a_y$ , at the spatial boundaries. Both when computing  $\sigma_x$  and  $\sigma_y$  we consider two different sets of boundary conditions as we now describe.

### Damping boundary conditions. Long systems

A reasonable boundary condition is derived from the assumption that the system is long enough for all the inhomogeneities sourced by the interface to die away towards the edges, that is from the requirement that the fluctuations become independent of  $x$  there, namely

$$\partial_x a_t(z, \pm L) = 0, \quad \partial_x c(z, \pm L) = 0, \quad (3.36)$$

while  $a_x$  is left free as discussed above.

To compute the conductivity in the direction parallel to the interface ( $\sigma_y$ ) we only need to solve for  $a_y$ . The damping boundary condition at the spatial boundaries is then

$$\partial_x a_y(z, \pm L) = 0. \quad (3.37)$$

### Boundary conditions. Short systems

One can instead be interested in a situation in which the system is not long enough for the inhomogeneities of the fluctuations to vanish towards the spatial boundaries. Consequently, a relaxation of the boundary conditions considered above for long systems would consist in allowing the fluctuations to have a nonzero derivative at the spatial boundary. Then, we must impose Dirichlet boundary conditions there. As discussed in the previous section,  $a_t$ , which is odd, must obey (3.34), hence an alternative boundary condition that allows for a nonzero  $\partial_x a_t$  at the boundary is

$$a_t(z, \pm L) = 0. \quad (3.38)$$

Analogously we require  $c$  to also vanish at the boundaries

$$c(z, \pm L) = 0. \quad (3.39)$$

Notice that these boundary conditions are nothing else than the requirement that  $a_t$  and  $c$  reach the solution of the homogeneous problem exactly at the edge. We should bear in mind that when computing the conductivity  $\sigma_x$  of an homogeneous system, only  $a_x$  has to be turned on, hence  $c$  and  $a_t$ , which decouple from  $a_x$ , vanish identically. It is straightforward to check, both analytically and numerically, that these boundary conditions are satisfied whenever the previous more restricting damping boundary conditions are imposed. Yet the opposite is not true, and for short enough systems the solutions are such that  $\partial_x a_t$  and  $\partial_x c$  are non-vanishing at the spatial boundaries.

Finally, for  $a_y$  one can also consider a Dirichlet boundary condition which requires that  $a_y$  reach the homogeneous solution at the boundary, namely the solution for  $a_y$  in a homogeneous background characterized by the values of the chemical potential and the mass far away from the interface

$$a_y(z, \pm L) = a_y^{\text{hom}}(z). \quad (3.40)$$

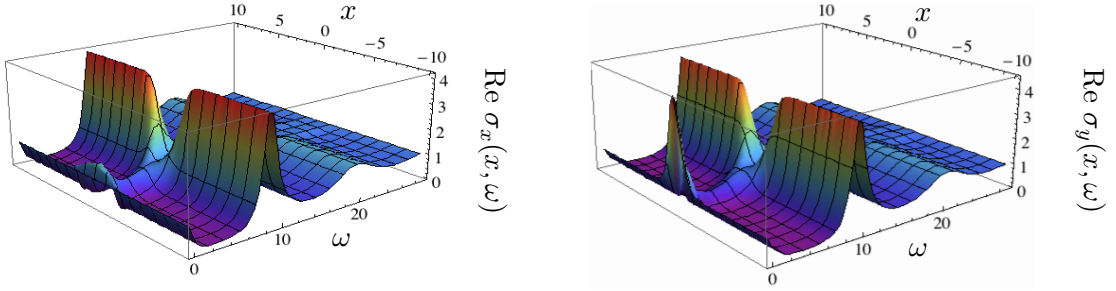


**Figure 6:** Real optical conductivities as a function of frequency and position, for a background with  $\mu = 4$  and  $m = 5.3$ . Notice that the main differences between  $\sigma_x$  and  $\sigma_y$  occur at low frequencies, and close to the interface ( $x = 0$ ).

Except for when we specifically focus on long systems (fig. 10), in the rest of this work we consider our systems to be short, and consequently impose the boundary conditions above. In particular, we set  $L = 10$  (remember  $x \in [-L, L]$ , with the interface located at  $x = 0$ ), and fix  $a = 3$  in (2.21), as discussed in section 2.4. Moreover, as for the background, we use grids of size  $50 \times 50$ , except for the results plotted in figures 7 and 8 which were obtained with a grid of size  $N_z \times N_x = 50 \times 35$ .

### 3.4 Results

Finally, in this section we present our results for the conductivities of a holographic interface. After a glance at the optical conductivity for the entire range of the coordinate  $x$ , we focus on its behavior at the interface. We end the section by studying the DC conductivity.

In figure 6 we plot the real part of the optical conductivities  $\sigma_x$  and  $\sigma_y$  as functions of the frequency  $\omega$ , and the position  $x$  for a background with  $\mu = 4$  and<sup>14</sup>  $M = 5.3$ . At intermediate and large frequencies, and away from the interface, both conductivities are very similar, not only to each other, but also to the conductivity of the equivalent homogeneous system, *i.e.* the one given by an homogeneous embedding with the same values of mass and chemical potential that characterize our system away from the interface. In particular, we observe the presence of the resonances given by the quasi-normal modes corresponding to the ‘melting’ vector mesons. In fact, as found in [65], the effective meson masses, which correspond to peaks in the spectral function, are in one-to-one relation with the frequencies

$$\omega_{\text{res}} = m\sqrt{2(k+1)(k+2)}, \quad k = 0, 1, 2, \dots, \quad (3.41)$$

which correspond to the masses of stable mesons [66]. Away from the interface the system becomes homogeneous, and therefore we expect the conductivity to reproduce the homogeneous result. On the other hand, near the interface the conductivities in the directions parallel and orthogonal to it behave quite differently, presenting interesting features which we elucidate below.

<sup>14</sup>We remind the reader that the value of  $M$  sets the mass reached by the inhomogeneous embedding (2.21) at the edges, away from the interface.

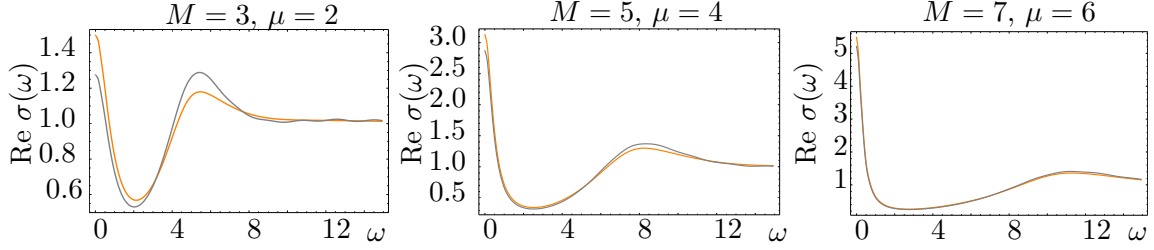


**Figure 7:** Plots of the real part of  $\sigma_y(\omega)$  (orange lines) at a point  $x = x_0 = 0.749$  in the vicinity of the interface for different pairs of values  $(M, \mu)$ . The gray line stands for the equivalent homogeneous conductivity  $\sigma_y^h(\omega)$ , obtained for an homogeneous system with the same mass  $m = m(x_0)$ , and chemical potential as our setup at that point (from left to right  $m(x_0) = 2.4262, 4.044$ , and  $5.661$  respectively).

Let us first study the effects of the inhomogeneities on the conductivity along the direction parallel to the interface. For a system like ours, homogeneous along the  $y$  direction, one could naively expect that at each point  $x$ , the conductivity in the  $y$  direction,  $\sigma_y(\omega, x)$ , be very similar to that of an homogeneous system having the same mass and chemical potential as our setup at that point, which we denote  $\sigma_y^h$ . However, as we discuss below,  $\sigma_y(\omega, x)$  is sensitive to the spatial gradients of the inhomogeneous embedding, and therefore becomes different from  $\sigma_y^h$  where the spatial gradients are large. To illustrate this, in figure 7 we plot  $\sigma_y(\omega)$  and  $\sigma_y^h(\omega)$  at the point where the difference between them is maximal, which is of course close to the interface. Interestingly, with respect to the equivalent homogeneous case we observe a transfer of spectral weight from intermediate to very low frequencies resulting in a larger DC conductivity in the presence of the interface. Moreover, we have checked that the relative enhancement increases with decreasing  $\mu$  for a given  $M$  as one moves toward the phase transition in the phase diagram 1.

The spatial gradients due to the interface affect the conductivity  $\sigma_y(\omega, x)$  in two ways. The most important effect occurs at the level of the background fields  $\chi$  and  $\phi$ : the nonzero spatial gradients of these fields result in a value of the charge density  $\rho(x)$ , which near the interface is higher than that of a homogeneous system with the same values of mass  $m(x)$  and chemical potential  $\mu$ . This is shown in the left panel of figure 8 where we compare both charge densities, and see that indeed, around the interface, the charge density of the inhomogeneous case is always larger. Consequently, one expects  $\sigma_y(x)$  and  $\sigma_y^h(x)$  to differ, and in particular, the DC value of  $\sigma_y(x)$  to be higher than that of  $\sigma_y^h$ . This is in agreement with what we see in fig. 7. Note that this effect, due to the enhancement of the charge density around the interface, would be there even if the form of the equations of motion for the fluctuations were not changed with respect to the homogeneous case. The second effect occurs at the level of the equations of motion of the fluctuations. Notice that while the fluctuation  $a_x$  is coupled to those of the embedding and the charge density,  $c$  and  $a_t$ , the field  $a_y$  decouples from any other fluctuation, as it happens in the homogeneous case. However, the DBI action does couple  $a_y$  to the spatial derivatives of the background functions,  $\dot{\phi}$  and  $\dot{\chi}$ , as can be seen in (B.2). Hence, there are new terms in the equation of

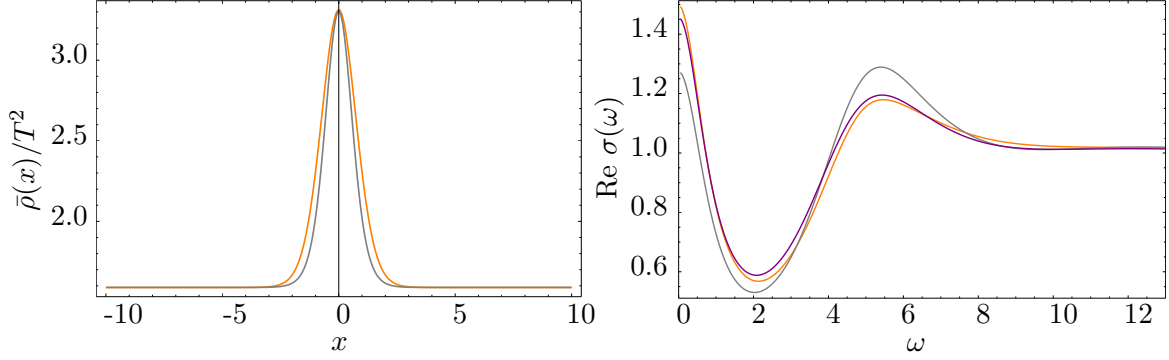


**Figure 8:** On the left panel we plot the charge density (orange line) for a setup with  $M = 3$  and  $\mu = 2$ . The gray line corresponds to the charge density of the equivalent homogeneous system at each point  $x$ , namely a homogeneous system with the same mass  $m(x)$  as our setup at that point. On the right we plot the same conductivities as in the leftmost plot of fig. 7 (orange and gray lines) together with the conductivity obtained for an homogeneous system with  $\mu = 3$  and  $m = 2.095$  (purple line). This last system has the same value of the charge density as the inhomogeneous setup at the point of interest ( $x = 0.749$ ).

motion for  $a_y$  that are not present in the homogeneous case, and one expects these terms to affect the conductivity. To try and gauge the relevance of these two effects, on the right panel of figure 8 we compare the conductivity  $\sigma_y(\omega)$ , computed at a point  $x$  (orange line), with the one that results for a system with the same value of the chemical potential and the charge density as our system at that point  $x$  (purple line). Although the purple line does not exactly overlap with the orange one, it is much closer to it than the gray line (which as in fig. 7 stands for  $\sigma_y^h$ ). This confirms that, as expected, the enhancement of the charge density due to the spatial inhomogeneities is the dominant effect of the interface on  $\sigma_y$ .

We now focus on the behavior of the conductivities at the interface. In figure 9 we plot both  $\sigma_x$  and  $\sigma_y$  at the interface for three different values of the background parameters  $M$  and  $\mu$ . We have chosen the pairs of values  $(M, \mu)$  so that they correspond to systems where the charge density at the edges is kept low (namely configurations at the edge of the area accessible to BH embeddings in fig. 1). At the interface the embedding becomes massless, thus the configurations with higher values of  $\mu = \bar{\mu}/T$  correspond to lower temperatures and higher values of the charge density.

By looking at the plots of the real part of the conductivities at the interface, presented on the right panels of figure 9, we observe one of the main features of our construction: the DC conductivity along the interface ( $\sigma_y^{\text{DC}}$ ) is considerably enhanced with respect to that in the direction perpendicular to it ( $\sigma_x^{\text{DC}}$ ). This is a direct consequence of the spatial distribution of the charge density in our system (see fig. 4 for an example of  $\rho(x)$ ). As we have seen in fig. 7, the conductivity  $\sigma_y(\omega)$  is basically determined by the value of the charge density at the point of interest, in this case  $x = 0$ . However, this is not the case for the conductivity in the  $x$  direction  $\sigma_x(\omega)$ . As we discuss below, when focusing on  $\sigma_x^{\text{DC}}$ ,



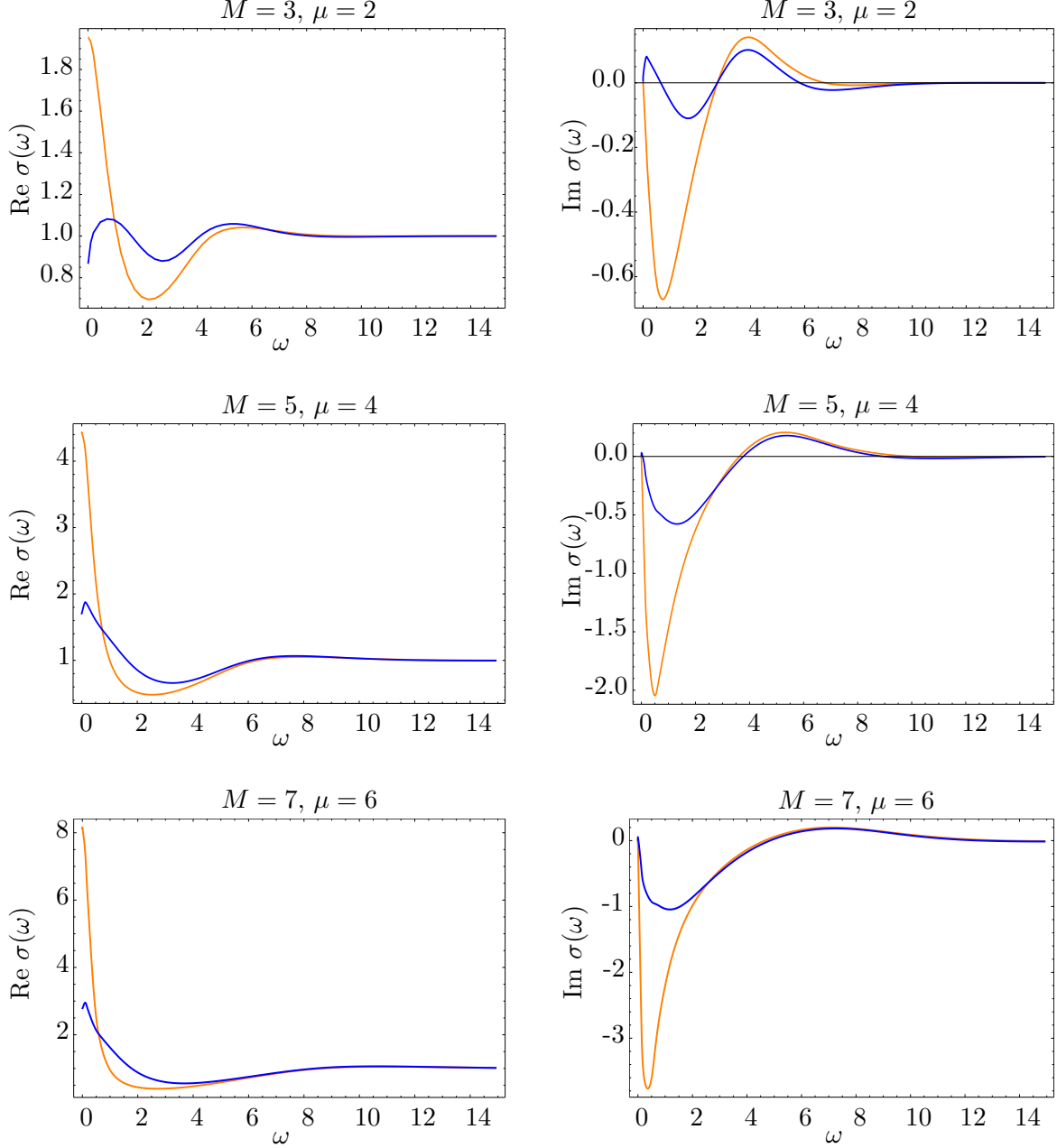


**Figure 9:** Conductivities at the interface. Plots of the conductivity  $\sigma_x(x=0, \omega)$  (blue) and  $\sigma_y(x=0, \omega)$  (orange) for different values of the background parameters  $M$  and  $\mu$ . The real parts are shown on the left and the imaginary parts on the right.

the DC conductivity along the  $x$  direction, which must be independent of  $x$  due to current conservation, is basically determined by the charge density at the edges of the system, which is much lower than that at the interface. Therefore  $\sigma_x^{\text{DC}}$  is suppressed with respect to  $\sigma_y(\omega)$ . This suppression is maximal for embeddings such that the charge density at the edges is arbitrarily small. Nevertheless,  $\sigma_x^{\text{DC}}$  never vanishes completely, since there is always a contribution from the thermally produced pairs of charge carriers [56].

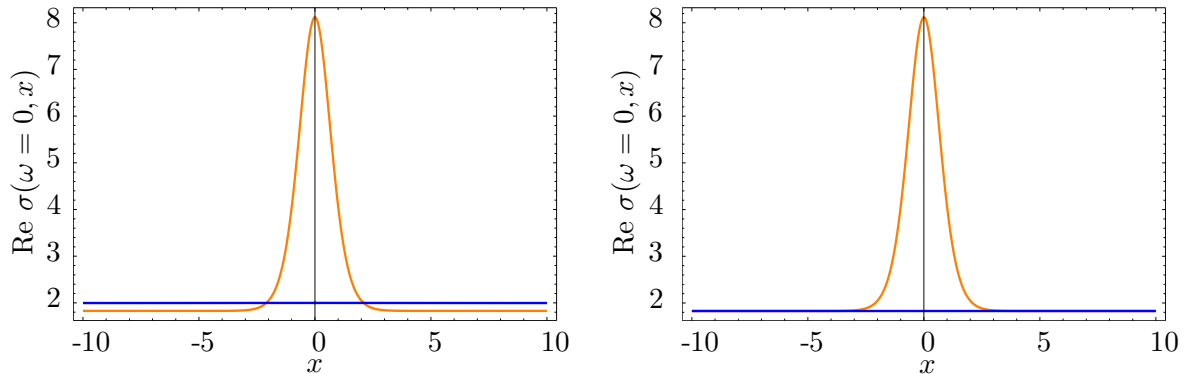


**Figure 10:** Comparison of  $\sigma_x^{DC}(x)$  (blue) and  $\sigma_y^{DC}(x)$  (orange) for a setup with  $\mu = 4$  and  $M = 5.3$ . On the left panel we plot the results for a short system, for which we set  $L = 10$ . The right panel corresponds to a long system where  $L = 100$ . In both cases we have set  $a = 3$  (remember that  $a$  determines the width of the interface via eq. (2.21)).

### 3.4.1 DC conductivity

In the following we focus on the DC conductivity along the direction orthogonal to the interface, namely  $\sigma_x^{DC}$ . As is obvious from the action of the fluctuations,  $\sigma_x$  is more sensitive to the effects of translational symmetry breaking introduced by our inhomogeneous embedding. In addition, as can be seen from the current conservation equation (3.14), for a setup like ours, in which the charge density does not vary with time,  $\sigma_x^{DC}$  is a constant. Moreover, as we have described in section 3.2, we can compute  $\sigma_x^{DC}$  from the behavior of the background functions at the horizon without having to solve the fluctuation equations in the  $\omega \rightarrow 0$  limit. Note that eq. (3.33) is particularly well suited to numerical evaluation for this purpose<sup>15</sup>.

We start by comparing the DC conductivities  $\sigma_x^{DC}$  and  $\sigma_y^{DC}$ . They are plotted in figure 10 for the two kinds of systems introduced in section 3.3. Let us first describe what we expect for  $\sigma_y^{DC}$ , and then discuss  $\sigma_x^{DC}$  in detail.

The DC conductivity along the direction parallel to the interface,  $\sigma_y^{DC}(x)$ , is read from the  $\omega \rightarrow 0$  limit of the AC conductivity  $\sigma_y(\omega, x)$ . As shown in fig. 7, up to a constant [56] and to some small effects sourced by the spatial gradients of the background,  $\sigma_y^{DC}(x)$  is determined by the value of the charge density at each point  $x$ . Hence, it is expected to peak at the interface, where the charge density is maximal, and to asymptote to a nonzero baseline value towards the edges.

In section 3.2 we discussed how to compute  $\sigma_x^{DC}$  in terms of the horizon data. Subsequently, in section 3.3 we defined two different kinds of systems corresponding to different boundary conditions for the fluctuations at the edges. As we now show, these result in slightly different behaviors of  $\sigma_x^{DC}$ .

<sup>15</sup>In fact, (3.33) is the expression we evaluate numerically to read the value of  $\sigma_x^{DC}$ . A field redefinition of the form  $\phi \rightarrow (1 - z)^2 \tilde{\phi}$  eliminates the need to evaluate a term containing a second derivative like  $a^{(2)}(x)$ .

## Long Systems

For these systems the effects of the interface fade away towards the edges. Consequently, in eq. (3.29) we can use the boundary condition (3.37), *i.e.*  $\partial_x p(\pm L) = \partial_x a_t(0, \pm L) = 0$  to get

$$\sigma_x^{\text{DC}} = \mathcal{F}(z = 1, x = \pm L), \quad (3.42)$$

which is the DC conductivity of a system without an interface, since  $\mathcal{F}$  at the edges agrees with that of a background with an homogeneous embedding. Notice that this is to be expected; assuming that the effects of the interface do not reach the edges amounts to having a system where the width of the interface is negligible with respect to the total length. Therefore we expect  $\sigma_x^{\text{DC}}$  to be the same as  $\sigma_y^{\text{DC}}(x = \pm L)$ , namely  $\sigma_y^{\text{DC}}$  at the edges.

On the right panel of figure 10 we plot  $\sigma_x^{\text{DC}}$  and  $\sigma_y^{\text{DC}}$  for a long system, and we observe that they overlap away from the interface.

## Short Systems

In section 3.3 we also considered the case of a system where the effects of the interface reach the boundary by allowing the derivatives of the fluctuations to be nonzero at the edges. In that case, it is still possible to compute  $\sigma_x^{\text{DC}}$  by means of the integral (3.32).

On the left panel of figure 10 we plot  $\sigma_x^{\text{DC}}$  and  $\sigma_y^{\text{DC}}$  for a short system. We see that  $\sigma_x^{\text{DC}}$  is slightly larger than  $\sigma_y^{\text{DC}}$  at the edges. The interface is now introducing a sizeable region where the charge density is augmented, producing a net enhancement of the conductivity  $\sigma_x^{\text{DC}}$ <sup>16</sup>.

In figure 11 we illustratively summarize the behavior of the DC conductivities in our system. As is clear from the illustration,  $\sigma_y^{\text{DC}}(x)$  roughly follows the charge density, which varies along  $x$  and peaks at the interface, while  $\sigma_x^{\text{DC}}$  is constant, its value mainly determined by the charge density away from the interface.

Finally, in figure 12 we study the evolution of  $\sigma_x^{\text{DC}}$  as a function of  $1/\mu = T/\bar{\mu}$ , at fixed  $M/\mu = M_q/\bar{\mu}$ . We perform the analysis for a short system with  $L = 10$ , and in order to study the effect of the interface, we compare  $\sigma_x^{\text{DC}}$  to the conductivity of an equivalent homogeneous system  $\sigma_{\text{DC}}^0$ . This is the DC conductivity for an homogeneous system with the same mass  $M$  and chemical potential  $\mu$  as our setup at its edges. Notice that for the values of  $M/\mu$  considered, there is a minimum value of  $1/\mu$  that can be reached by our embeddings (see fig. 2). Both conductivities grow as we lower the temperature ( $1/\mu$ ) until they reach a maximum, and then decrease rapidly. As is clear from the plots, the behavior of the conductivity follows closely that of the charge density at the edges (blue dashed line). Moreover,  $\sigma_x^{\text{DC}}$  is always slightly larger than the homogeneous counterpart  $\sigma_{\text{DC}}^0$  as expected

---

<sup>16</sup>In order to roughly estimate the DC conductivity  $\sigma_x^{\text{DC}}$ , we may think of the system as made of two regions: one region of length  $\epsilon$  and conductivity  $\sigma_{\text{DC}}^{\text{int}}$ , corresponding to the interface; and another region of length  $2L - \epsilon$  and conductivity  $\sigma_{\text{DC}}^0 < \sigma_{\text{DC}}^{\text{int}}$ , corresponding to the system away from the interface. One can then write  $\frac{2L}{\sigma_x^{\text{DC}}} = \frac{2L - \epsilon}{\sigma_{\text{DC}}^0} + \frac{\epsilon}{\sigma_{\text{DC}}^{\text{int}}}$ . Hence, when  $\epsilon \ll L$ ,  $\sigma_x^{\text{DC}} = \sigma_{\text{DC}}^0$ ; instead for  $\epsilon \lesssim L$ , we have  $\sigma_x^{\text{DC}} \gtrsim \sigma_{\text{DC}}^0$ . We point out that this analogy also works for non-symmetric systems, having  $m(x)$  interpolating between different masses at both sides of the interface.

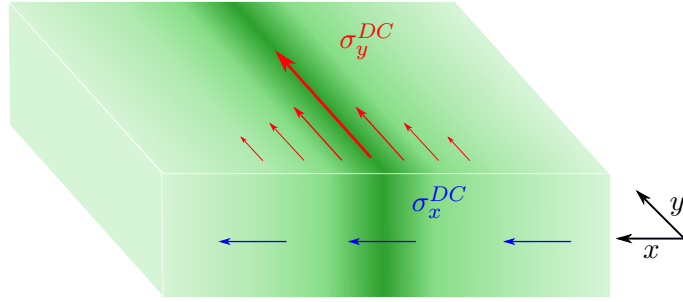


**Figure 11:** Schematic illustration of our setup. The system is two-dimensional; the third (vertical) dimension has been added for illustrative purposes. The intensity of green encodes the  $x$ -dependence of the charge density (see fig. 4), with darker green standing for larger charge density. The red arrows represent the value of  $\sigma_y^{DC}$ , which varies along the system, and the blue arrows denote the value of  $\sigma_x^{DC}$ , which is constant.

from the length of the system. Also note that, with respect to an homogeneous system, the presence of the interface has two competing effects on the DC conductivity. On the one hand, the interface is a region of small size where the charge density is much larger than in the homogeneous system towards the edges. This fact, as we have seen when discussing the plots in fig. 10, should result in an enhancement of  $\sigma_x^{DC}$ . On the other hand, the presence of the interface gives rise to inhomogeneities that, on general grounds, should impede the conductivity [59]. However, in view of our results the enhancement of the charge density is strong enough to overcome other effects of the inhomogeneous embedding.

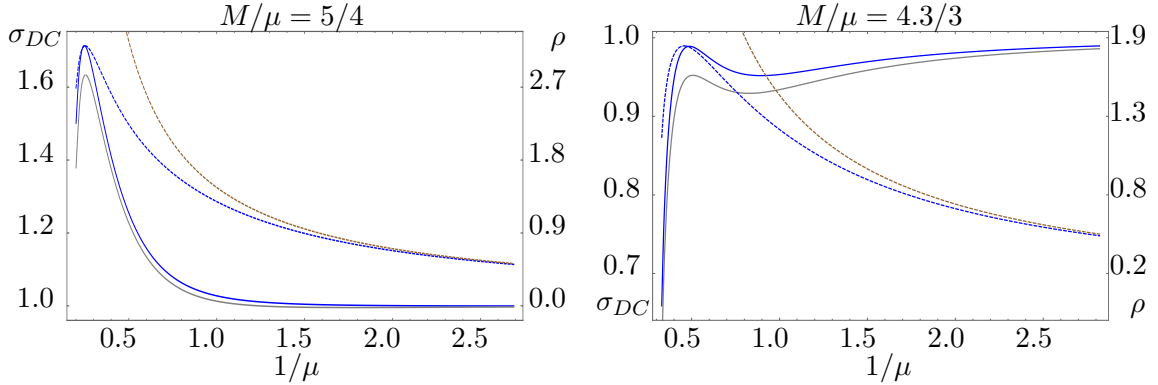


**Figure 12:** DC conductivity versus  $1/\mu = T/\bar{\mu}$ . The solid blue line corresponds to  $\sigma_x^{DC}$ , while the solid gray line represents  $\sigma_{DC}^0$ , which corresponds to a system with no interface. For guidance we also plot the values of the charge density at the edges (blue dashed lines) and at the interface (gray dashed lines). The left panel corresponds to a setup with  $\bar{\mu}/M_q = 4/5$ . The right panel is for  $\bar{\mu}/M_q = 3/4.3$ . The left vertical axes refer to the conductivity plots whereas the right ones show the scale for the charge density.

## 4 Conclusions

In this work we constructed a holographic system that realizes a one-dimensional charged interface. We have considered a D3/D5 intersection in the limit where the number of D5-branes is much smaller than that of D3-branes. The gravity dual consists of a probe D5-brane in the background generated by the D3-branes. We are interested in systems at fine temperature, which is why we have embedded the probe D5-brane in a black D3-brane geometry. Furthermore, in order to have a finite charge density of the fundamental degrees of freedom sourced by the D5-branes we switched on the temporal component of the worldvolume gauge field of the probe. Our configurations are massive embeddings for which the asymptotic distance between the D5-branes and the D3-branes is non-vanishing. The D5-brane is extended along two spatial Minkowski directions, giving rise to a (2+1)-dimensional defect. To realize the interface, we chose the mass parameter to depend on one of those Minkowski directions, which we denote by  $x$ , with a profile that interpolates between two homogeneous embeddings corresponding to a positive and negative mass respectively. Due to technical limitations arising from the numerics, our embeddings are chosen to be of black hole type for every value of  $x$ , thus the induced charge density is nonzero along the entire system. Nevertheless, the charge density peaks at the interface, where the mass vanishes, and away from it can be made arbitrarily small by appropriately tuning the embedding. To sum up, the embedding is described by two fields: the embedding scalar  $\chi$  and the temporal component of the worldvolume gauge field  $\phi$ . They both depend on the radial coordinate  $z$  and on the spatial direction  $x$ . The dynamics of the probe brane is governed by the DBI action and the equations of motion are a set of two coupled non-linear PDEs, for  $\chi$  and  $\phi$ . In order to construct our holographic interface we have solved those PDEs numerically.

For the configurations obtained in this way, we checked that indeed the charge density peaks at the interface. For the examples provided, the value of the charge density at the interface is about five times larger than at the edges. Moreover, both at the interface and away from it, we have studied the scaling of the charge density with the chemical potential, finding that it agrees with the result for the homogeneous intersection,  $\rho \propto \mu^2$  [64].

After constructing the backgrounds realizing the holographic interface, we proceeded with the computation of the electrical conductivities of the system. For this purpose, we studied the fluctuations of the worldvolume gauge field, which in some cases couple among themselves and with that of the scalar describing the embedding. We now summarize our main results.

We have computed the AC and DC conductivities both in the direction perpendicular to the interface ( $\sigma_x$ ) and in that parallel to it ( $\sigma_y$ ). As for the AC conductivities, away from the interface  $\sigma_x$  and  $\sigma_y$  do not present substantial differences and almost agree with the AC conductivity of an homogeneous system without interface. In particular, we observe the peaks due to mesonic excitations known from brane embeddings constant in  $x$ . These peaks disappear at the interface where the charge carriers become massless. Moreover, at the interface  $\sigma_x$  and  $\sigma_y$  present differences at low frequencies. Notice that low frequencies correspond to probing the system at long ranges, and for large length scales the setup looks

very different in the  $x$  and in the  $y$  direction.

Next, we studied the effects of the inhomogeneous background on the conductivity in the direction parallel to the interface,  $\sigma_y$ . Despite the background being homogeneous along the  $y$  direction, due to the non-linearities of the DBI action, a current along  $y$  is sensitive to the gradients along  $x$  of the background fields  $\chi$  and  $\phi$ . These gradients are larger in the vicinity of the interface, and therefore have more significant effects upon the conductivity  $\sigma_y$  in this region. We have checked that the main effect of these gradients on the conductivity  $\sigma_y$  is due to an enhancement of the charge density with respect to what would be the equivalent homogeneous system. In particular, we found that close to the interface the inhomogeneous background causes a transfer of spectral weight from mid to low frequencies, resulting in an enhancement of the DC conductivity  $\sigma_y^{\text{DC}}$ .

We have paid special attention to the computation of the DC conductivity in the direction perpendicular to the interface,  $\sigma_x^{\text{DC}}$ . For a system like the one at hand, where the charge density is inhomogeneous only in the  $x$  direction, current conservation implies that  $\sigma_x^{\text{DC}}$  is constant. Moreover, following [58, 59], we were able to compute  $\sigma_x^{\text{DC}}$  in terms of the background fields evaluated at the horizon. Two of the most relevant results of this work are related to the conductivity  $\sigma_x^{\text{DC}}$ .

An important feature of our system is the fact that  $\sigma_x^{\text{DC}}$  is basically determined by the homogeneous system away from the interface, where the charge density is very low. On the other hand,  $\sigma_y^{\text{DC}}$  varies with  $x$  and is roughly proportional to the charge density. Consequently, at the interface the conductivity along it,  $\sigma_y^{\text{DC}}$ , is considerably larger than the conductivity in the orthogonal direction,  $\sigma_x^{\text{DC}}$ . For some of our numerical simulations,  $\sigma_y^{\text{DC}}$  at the interface is up to  $4 \times \sigma_x^{\text{DC}}$ .

Our analysis of  $\sigma_x^{\text{DC}}$  provides information on the effects of the breaking of translational symmetry caused by our interface. In particular, we showed that when the size of the inhomogeneous region is not negligible with respect to the total size of the system,  $\sigma_x^{\text{DC}}$  is sensitive to the inhomogeneities. Interestingly, two competing effects are expected to be at work in this scenario: the increase of charge density at the interface is expected to cause an increase of  $\sigma_x^{\text{DC}}$ , while the non-vanishing gradient of the charge density along  $x$  ought to suppress the conductivity [59]. In the light of our results, we see the effect of charge density localization being clearly dominant for our setup. Additionally, we studied the evolution of  $\sigma_x^{\text{DC}}$  with the temperature, and found it to be always larger than its homogeneous counterpart, with the increment becoming larger at lower temperatures.

To conclude, let us comment on some possible applications of the holographic interface studied in this work. The D3/D5 intersection with a kink profile for the embedding was proposed in [37] as the holographic realization of Quantum Spin Hall (QSH) insulators. A key feature of these systems is a non-vanishing mixed Chern-Simons term of the form  $A^R \wedge dA$ . The gauge field  $A^R$  corresponds to a  $U(1)$   $R$ -symmetry, which in this condensed matter systems is associated to the  $U(1)$  spin global symmetry, i.e. the  $z$  component of the spin of the electrons. In the holographic dual, the  $U(1)_R$  corresponds to a shift symmetry of the internal  $S^5$ , and the gauge field  $A^R$  appears as a fluctuation of the RR four-form  $C_4$  [67]. A non-trivial WZ term of the form  $A^R \wedge dA$  is generated when fluctuations of the  $C_4$  are considered. It would therefore be interesting to extend the analysis of this work to

the case in which a topological term as described above is present. This would allow for a study of the QSH conductivity in a (2+1)-dimensional topological insulator.

Another interesting continuation of our work would be the extension of our analysis to the case of the holographic (3+1)-dimensional topological insulators constructed in [36] by means of a D3/D7 intersection. That system consists of a D7-brane probe with an inhomogeneous embedding as the one studied here. In that case a nonzero WZ term is generated at the interface, sourcing a finite Hall conductivity. The relevant D7-brane embeddings at finite temperature and charge density were constructed in [41], and the next natural step would be the repetition of the analysis of the conductivity presented here for those D7-brane embeddings. A crucial difference would arise from the nonzero Hall conductivity around the interface. Since the embeddings at finite charge density are always of black hole type, this model would describe the electric transport at the transition between different quantum Hall states, see [68].

A further continuation of this work would consist in trying to ascertain the existence of purely fermionic massless degrees of freedom at the interface. For a embedding with a step-like profile, at the interface the D5-brane shares only one spatial direction with the D3-branes, and therefore the intersection becomes of the D3/D5' type. For this intersection, with six mixed boundary conditions on the worldsheet ( $\#ND = 6$ ), the only fundamental massless degrees of freedom in the spectrum are fermionic. Hence it would be interesting to study the Green's functions of different (gauge invariant) operators at such an interface, and look for signatures of the existence of a Fermi surface.

Finally, as proposed in [59], setups involving inhomogeneous brane intersections may be used to study the effects of disorder on strongly coupled systems at finite charge density. An example for this is provided by intersections where the chemical potential is given by an inhomogeneous profile with random fluctuations around a baseline value, as in [13]. This is a direction of work we are actively pursuing and we expect to report on our results in the future.

## Acknowledgments

It is a pleasure to thank M. Ammon, O. Bergman, A. Donos, M. Jarvinen, A. Karch, G. Lifshytz, C. Pantelidou, M. Pérez-Victoria, M. Rozali, I. Salazar, J. Tarrío, M. Yunpu and H. Zeller for useful discussions. D.A. thanks the FRont Of pro-Galician Scientists for unconditional support. The work of D. Areán is supported by the German-Israeli Foundation (GIF), grant 1156. The work of J.M. Lizana is supported by MINECO, via the FPI program, and projects FPA2010-17915 and FPA2013-47836-C3-2-P and by the Junta de Andalucía projects FQM 101 and FQM 6552.

## A Background equations of motion

In this appendix we write down the equations of motion of the background functions, namely those for the functions  $\chi(z, x)$  and  $\phi(z, x)$  describing the embedding of the probe

D5-brane. They follow from the action (2.10), and take the form

$$\eta_1(\partial_z^2\phi) + \eta_2(\partial_x^2\phi) + \eta_3(\partial_z\partial_x\phi) + \eta_4(\partial_z\phi)^3 + \eta_5(\partial_z\chi\partial_x\chi\partial_x\phi) + \eta_6(\partial_z\phi) = 0, \quad (\text{A.1})$$

$$\begin{aligned} \tau_1(\partial_z^2\chi) + \tau_2(\partial_x^2\chi) + \tau_3(\partial_z\partial_x\chi) + \tau_4(\partial_z\chi)^3 + \tau_5(\partial_z\chi)^2 + \tau_6(\partial_z\chi) + \tau_7(\partial_x\chi)^2 \\ + \tau_8(\partial_x\chi) + \tau_9\chi = 0, \end{aligned} \quad (\text{A.2})$$

where the coefficients  $\eta_i$ , ( $i = 1 \dots 7$ ), and  $\tau_i$ , ( $i = 1 \dots 9$ ), are given by the following functions of  $z$  and  $x$ ,

$$\begin{aligned} \eta_1(z, x) &= 2h \left[ hz^4(1 - \chi^2)\dot{\phi}^2 - f^2(h(1 - \chi^2) + z^2\dot{\chi}^2) \right], \\ \eta_2(z, x) &= 2h \left[ hz^4(1 - \chi^2)\phi'^2 - f^2(1 - \chi^2 + z^2\chi'^2) \right], \\ \eta_3(z, x) &= 4hz^2 \left[ f^2\chi'\dot{\chi} - hz^2(1 - \chi^2)\phi'\dot{\phi} \right], \\ \eta_4(z, x) &= hz^3(zh' - 2h) \left[ 2h(1 - \chi^2) + z^2\dot{\chi}^2 \right], \\ \eta_5(z, x) &= 4fhz(2f - zf') + 2hz^5\phi'^2(2h - zh'), \\ \eta_6(z, x) &= hz^3\dot{\phi}^2 \left[ -h(4(1 - \chi^2) + 2z^2\chi'^2) + zh'(3(1 - \chi^2) + z^2\chi'^2) \right] \\ &\quad - 2fhf' \left[ -z^2\dot{\chi}^2 - h(1 - \chi^2 - z^2\chi'^2) \right] + f^2 \left[ -2z^2\dot{\chi}^2h' + 6h^2z\chi'^2 \right. \\ &\quad \left. + h(-2z\dot{\chi}^2 - h'(3(1 - \chi^2) + z^2\chi'^2)) \right] \end{aligned} \quad (\text{A.3})$$

$$\begin{aligned} \tau_1(z, x) &= 2hz^2 \left[ hz^4(1 - \chi^2)\dot{\phi}^2 - f^2(h(1 - \chi^2) + z^2\dot{\chi}^2) \right], \\ \tau_2(z, x) &= 2hz^2 \left[ hz^4(1 - \chi^2)\phi'^2 - f^2(1 - \chi^2 + z^2\chi'^2) \right], \\ \tau_3(z, x) &= 4hz^4 \left[ f^2\chi'\dot{\chi} - hz^2\phi'\dot{\phi}(1 - \chi^2) \right], \\ \tau_4(z, x) &= hz^3 \left[ 6f^2h - 2fhzf' - 2hz^4\dot{\phi}^2 - zh'(f^2 - z^4\dot{\phi}^2) \right] \\ \tau_5(z, x) &= 6h^2z^2\chi(-f^2 + z^4\dot{\phi}^2) + 2hz^7\phi'(2h - zh')\dot{\phi}\dot{\chi}, \\ \tau_6(z, x) &= z \left\{ -2fhz(h(1 - \chi^2) + z^2\dot{\chi}^2)f' + f^2[4h^2(1 - \chi^2) - 2z^3\dot{\chi}^2h' \right. \\ &\quad \left. + hz(6z\dot{\chi}^2 - (1 - \chi^2)h')] + hz^4[-2h\phi'(6z\chi\dot{\phi}\dot{\chi} - 2h\chi^2\phi' + (2h + z^2\dot{\chi}^2)) \right. \\ &\quad \left. + zh'((1 - \chi^2)\dot{\phi}^2 + (2h(1 - \chi^2) + z^2\dot{\chi}^2)\phi'^2) \right\} \\ \tau_7(z, x) &= 6hz^2\chi(hz^4\phi'^2 - f^2), \\ \tau_8(z, x) &= -2hz^5(1 - \chi^2)(2h - zh')\phi'\dot{\phi}, \\ \tau_9(z, x) &= 4h^2 \left[ z^4(\dot{\phi}^2 + h\phi'^2) - f^2 \right], \end{aligned} \quad (\text{A.4})$$

where primes stand for derivatives with respect to  $z$ , and dots for derivatives with respect to  $x$ .

## B Quadratic action for the fluctuations

In this appendix we present the action of the fluctuations considered in section 3.1, and which allowed us to compute the conductivity of the setup. The action results from ex-



panding the DBI action up to second order in the fluctuations (3.2), and can be written as

$$S^{(2)} = -N_f T_{D5} L^6 \int dt d^2x dz d\Omega_2 \mathcal{L}^{(2)}, \quad (\text{B.1})$$

with

$$\begin{aligned} \mathcal{L}^{(2)} = & -\Delta \left\{ \left[ c\Upsilon\chi - z^2(1-\chi^2)(1-\chi^2)(a'_t - i\omega a_z)h^2 z^2 \dot{\phi} - f^2 \chi' \dot{c} + h \left( z^4 \dot{\phi} \dot{c} (\dot{\phi} \chi' - \dot{\chi} \phi') \right. \right. \right. \\ & - c' \left( \dot{\chi} (f^2 - z^4 \phi'^2) + z^4 \dot{\phi} \phi' \chi' \right) + z^4 \chi' (\dot{\phi} \chi' - \dot{\chi} \phi') (a'_t - i\omega a_z) \\ & \left. \left. + \left( z^4 \dot{\phi} \dot{\chi} \chi' - z^2(1-\chi^2 + z^2 \dot{\chi}^2) \right) (i\omega a_x - \dot{a}_t) \right) \right]^2 \\ & - \frac{\Sigma}{h(1-\chi^2)} \left[ \Omega h c^2 - 4h z^2 \chi c \dot{c} \left( h z^4 \chi' \dot{\phi}^2 - f^2 \chi' - h z^4 \dot{\phi} \dot{\chi} \phi' \right) \right. \\ & - h \left( z^4 \dot{\phi} \phi' \chi' + \dot{\chi} (f^2 - z^4 \phi'^2) \right) c' + h z^2 \left( \dot{\phi} (2h(1-\chi^2) + z^2 \chi'^2) - z^2 \dot{\chi} \phi' \chi' \right) (a'_t - i\omega a_z) \\ & + \left( h z^4 \dot{\phi} \dot{\chi} \chi' - h z^2 (2 - 2\chi^2 + z^2 \dot{\chi}^2) \right) (i\omega a_x - \dot{a}_t) \\ & - z^2(1-\chi^2) \left( h^3 (2z^2 i\omega (1-\chi^2) a'_t a_z - z^2(1-\chi^2) a_t'^2 + \omega^2 (c^2 + z^2(1-\chi^2)) a_z^2) \right. \\ & + f^2 z^2 \left( z^2 \chi'^2 a_y'^2 - 2z^2 \dot{\chi} \chi' a_y' \dot{a}_y + (1-\chi^2 + z^2 \dot{\chi}^2) \dot{a}_y^2 \right) + h \left( f^2 z^2 (1-\chi^2) a_x'^2 + f^2 \dot{c}^2 \right. \\ & + z^2(1-\chi^2) (f^2 - z^4 \phi'^2) a_y'^2 + z^4 \omega^2 \chi'^2 a_y^2 + 2z^6 (1-\chi^2) \dot{\phi} \phi' a_y' \dot{a}_y - z^6 \dot{\phi}^2 \dot{a}_y^2 + z^6 \chi^2 \dot{\phi}^2 \dot{a}_y^2 \\ & - 2f^2 z^2 (1-\chi^2) a_x' a_z' + f^2 z^2 a_z'^2 - f^2 z^2 \chi^2 a_z'^2 \left. \right) - h^2 \left( 2z^4 \dot{\phi} \phi' c' \dot{c} - (f^2 - z^4 \phi'^2) c'^2 \right. \\ & - \phi' \chi' (a'_t - i\omega a_z) + (\dot{\phi} \chi' - 2\dot{\chi} \phi') (i\omega a_x - \dot{a}_t) \\ & + z^2 \left( z^2 \dot{\phi}^2 \dot{c}^2 + 2z^2 \dot{\chi} \phi' (i\omega c a_x' - \dot{c} a_t' + i\omega \dot{c} a_z) - (1-\chi^2 + z^2 \dot{\chi}^2) \omega^2 (a_x^2 + a_y^2) \right. \\ & + 2z^2 \dot{\phi} \chi' (2\dot{c} a_t' - i\omega \dot{c} a_z - i\omega c a_x') + z^2 \chi'^2 (a_t'^2 - 2i\omega a_t' a_z - \omega^2 a_z^2) \\ & + 2z^2 \dot{\phi} \dot{\chi} ((i\omega a_x - \dot{a}_t) \dot{c}) - 2z^2 \dot{\chi} \chi' ((i\omega a_z - a_t') (i\omega a_x - \dot{a}_t)) \\ & \left. \left. + (1-\chi^2 + z^2 \dot{\chi}^2) (\dot{a}_t^2 - 2i\omega a_x \dot{a}_t) - 2z^2 (\dot{\chi} \phi' + \dot{\phi} \chi') i\omega c a_z \right) \right] \right\}, \quad (\text{B.2}) \end{aligned}$$

where

$$\Delta = \frac{1}{2 z^{16} \mathcal{L}^{(0)3}}, \quad (\text{B.3})$$

$\mathcal{L}^{(0)}$  being the Lagrangian of the zeroth order DBI action, (2.10) and the functions  $\Upsilon$ ,  $\Sigma$  and  $\Omega$  are defined as

$$\begin{aligned} \Upsilon = & h z^4 \left[ (2 - 2\chi^2 + z^2 \dot{\chi}^2) \phi'^2 - 2z^2 \dot{\phi} \dot{\chi} \phi' \chi' + (2h(1 - \chi^2) + z^2 \chi'^2) \dot{\phi}^2 \right] \\ & - f^2 \left[ h(2 - 2\chi^2 + z^2 \dot{\chi}^2) + z^2 \chi'^2 \right], \end{aligned} \quad (\text{B.4})$$

$$\begin{aligned} \Sigma = & (1 - \chi^2)^2 \left\{ h z^4 \left[ (1 - \chi^2 + z^2 \dot{\chi}^2) \phi'^2 - 2z^2 \dot{\phi} \dot{\chi} \phi' \chi' + (h(1 - \chi^2) + z^2 \chi'^2) \dot{\phi}^2 \right] \right. \\ & \left. - f^2 \left[ h(1 - \chi^2 + z^2 \dot{\chi}^2) + z^2 \chi'^2 \right] \right\}, \end{aligned} \quad (\text{B.5})$$

$$\begin{aligned} \Omega = & \left\{ h z^4 \left[ (2 - 6\chi^2 + z^2 \dot{\chi}^2) \phi'^2 - 2z^2 \dot{\phi} \dot{\chi} \phi' \chi' + (2h(1 - 3\chi^2) + z^2 \chi'^2) \dot{\phi}^2 \right] \right. \\ & \left. - f^2 \left[ h(2 - 6\chi^2 + z^2 \dot{\chi}^2) + z^2 \chi'^2 \right] \right\}. \end{aligned} \quad (\text{B.6})$$

Note that we gauge away the radial gauge field component  $a_z$  once the equations of motion for the fluctuation fields have been found.

## References

- [1] J. M. Maldacena, *The Large N limit of superconformal field theories and supergravity*, *Adv.Theor.Math.Phys.* **2** (1998) 231–252 [[hep-th/9711200](#)].
- [2] E. Witten, *Anti-de Sitter space and holography*, *Adv.Theor.Math.Phys.* **2** (1998) 253–291 [[hep-th/9802150](#)].
- [3] S. Gubser, I. R. Klebanov and A. M. Polyakov, *Gauge theory correlators from noncritical string theory*, *Phys.Lett.* **B428** (1998) 105–114 [[hep-th/9802109](#)].
- [4] O. Aharony, S. S. Gubser, J. M. Maldacena, H. Ooguri and Y. Oz, *Large N field theories, string theory and gravity*, *Phys.Rept.* **323** (2000) 183–386 [[hep-th/9905111](#)].
- [5] S. Kachru, A. Karch and S. Yaida, *Holographic Lattices, Dimers, and Glasses*, *Phys.Rev.* **D81** (2010) 026007 [[0909.2639](#)].
- [6] S. Kachru, A. Karch and S. Yaida, *Adventures in Holographic Dimer Models*, *New J.Phys.* **13** (2011) 035004 [[1009.3268](#)].
- [7] G. T. Horowitz, J. E. Santos and D. Tong, *Optical Conductivity with Holographic Lattices*, *JHEP* **1207** (2012) 168 [[1204.0519](#)].
- [8] G. T. Horowitz, J. E. Santos and D. Tong, *Further Evidence for Lattice-Induced Scaling*, *JHEP* **1211** (2012) 102 [[1209.1098](#)].
- [9] G. T. Horowitz and J. E. Santos, *General Relativity and the Cuprates*, *JHEP* **1306** (2013) 087 [[1302.6586](#)].
- [10] M. Blake, D. Tong and D. Vegh, *Holographic Lattices Give the Graviton an Effective Mass*, *Phys.Rev.Lett.* **112** (2014), no. 7 071602 [[1310.3832](#)].
- [11] S. A. Hartnoll and J. E. Santos, *Cold planar horizons are floppy*, *Phys.Rev.* **D89** (2014), no. 12 126002 [[1403.4612](#)].
- [12] A. Donos and J. P. Gauntlett, *The thermoelectric properties of inhomogeneous holographic lattices*, [1409.6875](#).

- [13] D. Arean, A. Farahi, L. A. Pando Zayas, I. S. Landea and A. Scardicchio, *A Dirty Holographic Superconductor*, *Phys.Rev.* **D89** (2014) 106003 [[1308.1920](#)].
- [14] D. Arean, A. Farahi, L. A. Pando Zayas, I. S. Landea and A. Scardicchio, *Holographic p-wave Superconductor with Disorder*, [1407.7526](#).
- [15] S. A. Hartnoll and J. E. Santos, *Disordered horizons: Holography of randomly disordered fixed points*, *Phys.Rev.Lett.* **112** (2014) 231601 [[1402.0872](#)].
- [16] S. A. Hartnoll, D. M. Ramirez and J. E. Santos, *Emergent scale invariance of disordered horizons*, [1504.03324](#).
- [17] S. R. Coleman, *Q Balls*, *Nucl.Phys.* **B262** (1985) 263.
- [18] A. Donos and J. P. Gauntlett, *Holographic Q-lattices*, *JHEP* **1404** (2014) 040 [[1311.3292](#)].
- [19] A. Donos and J. P. Gauntlett, *Novel metals and insulators from holography*, *JHEP* **1406** (2014) 007 [[1401.5077](#)].
- [20] Y. Ling, P. Liu, C. Niu, J.-P. Wu and Z.-Y. Xian, *Holographic Superconductor on Q-lattice*, *JHEP* **1502** (2015) 059 [[1410.6761](#)].
- [21] T. Andrade and B. Withers, *A simple holographic model of momentum relaxation*, *JHEP* **1405** (2014) 101 [[1311.5157](#)].
- [22] B. Gout  raux, *Charge transport in holography with momentum dissipation*, *JHEP* **1404** (2014) 181 [[1401.5436](#)].
- [23] E. Mefford and G. T. Horowitz, *Simple holographic insulator*, *Phys.Rev.* **D90** (2014), no. 8 084042 [[1406.4188](#)].
- [24] M. Taylor and W. Woodhead, *Inhomogeneity simplified*, [1406.4870](#).
- [25] K.-Y. Kim, K. K. Kim, Y. Seo and S.-J. Sin, *Coherent/incoherent metal transition in a holographic model*, *JHEP* **1412** (2014) 170 [[1409.8346](#)].
- [26] R. A. Davison and B. Gout  raux, *Momentum dissipation and effective theories of coherent and incoherent transport*, *JHEP* **1501** (2015) 039 [[1411.1062](#)].
- [27] T. Andrade and S. A. Gentle, *Relaxed superconductors*, [1412.6521](#).
- [28] R. A. Davison and B. Gout  raux, *Dissecting holographic conductivities*, [1505.05092](#).
- [29] N. Iizuka, S. Kachru, N. Kundu, P. Narayan, N. Sircar *et. al.*, *Bianchi Attractors: A Classification of Extremal Black Brane Geometries*, *JHEP* **1207** (2012) 193 [[1201.4861](#)].
- [30] N. Iizuka, S. Kachru, N. Kundu, P. Narayan, N. Sircar *et. al.*, *Extremal Horizons with Reduced Symmetry: Hyperscaling Violation, Stripes, and a Classification for the Homogeneous Case*, *JHEP* **1303** (2013) 126 [[1212.1948](#)].
- [31] A. Donos and J. P. Gauntlett, *Holographic helical superconductors*, *JHEP* **1112** (2011) 091 [[1109.3866](#)].
- [32] A. Donos and J. P. Gauntlett, *Helical superconducting black holes*, *Phys.Rev.Lett.* **108** (2012) 211601 [[1203.0533](#)].
- [33] A. Donos and S. A. Hartnoll, *Interaction-driven localization in holography*, *Nature Phys.* **9** (2013) 649–655 [[1212.2998](#)].
- [34] Y.-Y. Bu, J. Erdmenger, J. P. Shock and M. Strydom, *Magnetic field induced lattice ground states from holography*, *JHEP* **1303** (2013) 165 [[1210.6669](#)].

- [35] B. Withers, *Holographic Checkerboards*, *JHEP* **1409** (2014) 102 [[1407.1085](#)].
- [36] C. Hoyos-Badajoz, K. Jensen and A. Karch, *A Holographic Fractional Topological Insulator*, *Phys.Rev.* **D82** (2010) 086001 [[1007.3253](#)].
- [37] A. Karch, J. Maciejko and T. Takayanagi, *Holographic fractional topological insulators in 2+1 and 1+1 dimensions*, *Phys.Rev.* **D82** (2010) 126003 [[1009.2991](#)].
- [38] J. Maciejko, X.-L. Qi, A. Karch and S.-C. Zhang, *Fractional topological insulators in three dimensions*, *Phys.Rev.Lett.* **105** (2010) 246809 [[1004.3628](#)].
- [39] R. Jackiw and C. Rebbi, *Solitons with Fermion Number 1/2*, *Phys.Rev.* **D13** (1976) 3398–3409.
- [40] J. Callan, Curtis G. and J. A. Harvey, *Anomalies and Fermion Zero Modes on Strings and Domain Walls*, *Nucl.Phys.* **B250** (1985) 427.
- [41] M. Rozali, *Compressible Matter at an Holographic Interface*, *Phys.Rev.Lett.* **109** (2012) 231601 [[1210.0029](#)].
- [42] M. Ammon and M. Gutperle, *A supersymmetric holographic dual of a fractional topological insulator*, *Phys.Rev.* **D86** (2012) 025018 [[1204.2217](#)].
- [43] O. Aharony, A. Fayyazuddin and J. M. Maldacena, *The Large N limit of N=2, N=1 field theories from three-branes in F theory*, *JHEP* **9807** (1998) 013 [[hep-th/9806159](#)].
- [44] A. Karch and E. Katz, *Adding flavor to AdS / CFT*, *JHEP* **0206** (2002) 043 [[hep-th/0205236](#)].
- [45] A. Karch and L. Randall, *Open and closed string interpretation of SUSY CFT's on branes with boundaries*, *JHEP* **0106** (2001) 063 [[hep-th/0105132](#)].
- [46] O. DeWolfe, D. Z. Freedman and H. Ooguri, *Holography and defect conformal field theories*, *Phys.Rev.* **D66** (2002) 025009 [[hep-th/0111135](#)].
- [47] J. Erdmenger, Z. Guralnik and I. Kirsch, *Four-dimensional superconformal theories with interacting boundaries or defects*, *Phys.Rev.* **D66** (2002) 025020 [[hep-th/0203020](#)].
- [48] K. Jensen, A. Karch and E. G. Thompson, *A Holographic Quantum Critical Point at Finite Magnetic Field and Finite Density*, *JHEP* **1005** (2010) 015 [[1002.2447](#)].
- [49] J. Babington, J. Erdmenger, N. J. Evans, Z. Guralnik and I. Kirsch, *Chiral symmetry breaking and pions in nonsupersymmetric gauge / gravity duals*, *Phys.Rev.* **D69** (2004) 066007 [[hep-th/0306018](#)].
- [50] D. Mateos, R. C. Myers and R. M. Thomson, *Holographic phase transitions with fundamental matter*, *Phys.Rev.Lett.* **97** (2006) 091601 [[hep-th/0605046](#)].
- [51] N. Evans and E. Threlfall, *Chemical Potential in the Gravity Dual of a 2+1 Dimensional System*, *Phys.Rev.* **D79** (2009) 066008 [[0812.3273](#)].
- [52] C. Hoyos-Badajoz, K. Landsteiner and S. Montero, *Holographic meson melting*, *JHEP* **0704** (2007) 031 [[hep-th/0612169](#)].
- [53] S. Kobayashi, D. Mateos, S. Matsuura, R. C. Myers and R. M. Thomson, *Holographic phase transitions at finite baryon density*, *JHEP* **0702** (2007) 016 [[hep-th/0611099](#)].
- [54] D. Mateos, S. Matsuura, R. C. Myers and R. M. Thomson, *Holographic phase transitions at finite chemical potential*, *JHEP* **0711** (2007) 085 [[0709.1225](#)].

- [55] S. Nakamura, Y. Seo, S.-J. Sin and K. Yogendran, *Baryon-charge Chemical Potential in AdS/CFT*, *Prog.Theor.Phys.* **120** (2008) 51–76 [[0708.2818](#)].
- [56] A. Karch and A. O’Bannon, *Metallic AdS/CFT*, *JHEP* **0709** (2007) 024 [[0705.3870](#)].
- [57] S. A. Hartnoll, J. Polchinski, E. Silverstein and D. Tong, *Towards strange metallic holography*, *JHEP* **1004** (2010) 120 [[0912.1061](#)].
- [58] N. Iqbal and H. Liu, *Universality of the hydrodynamic limit in AdS/CFT and the membrane paradigm*, *Phys.Rev.* **D79** (2009) 025023 [[0809.3808](#)].
- [59] S. Ryu, T. Takayanagi and T. Ugajin, *Holographic Conductivity in Disordered Systems*, *JHEP* **1104** (2011) 115 [[1103.6068](#)].
- [60] M. Rangamani, M. Rozali and D. Smyth, *Spatial Modulation and Conductivities in Effective Holographic Theories*, [1505.05171](#).
- [61] D. Arean and A. V. Ramallo, *Open string modes at brane intersections*, *JHEP* **0604** (2006) 037 [[hep-th/0602174](#)].
- [62] R. C. Myers and R. M. Thomson, *Holographic mesons in various dimensions*, *JHEP* **0609** (2006) 066 [[hep-th/0605017](#)].
- [63] J. Erdmenger, N. Evans, I. Kirsch and E. Threlfall, *Mesons in Gauge/Gravity Duals - A Review*, *Eur.Phys.J.* **A35** (2008) 81–133 [[0711.4467](#)].
- [64] F. Nogueira and J. B. Stang, *Density versus chemical potential in holographic field theories*, *Phys.Rev.* **D86** (2012) 026001 [[1111.2806](#)].
- [65] J. Erdmenger, M. Kaminski and F. Rust, *Holographic vector mesons from spectral functions at finite baryon or isospin density*, *Phys.Rev.* **D77** (2008) 046005 [[0710.0334](#)].
- [66] M. Kruczenski, D. Mateos, R. C. Myers and D. J. Winters, *Meson spectroscopy in AdS / CFT with flavor*, *JHEP* **0307** (2003) 049 [[hep-th/0304032](#)].
- [67] O. Aharony, J. Pawelczyk, S. Theisen and S. Yankielowicz, *A Note on anomalies in the AdS / CFT correspondence*, *Phys.Rev.* **D60** (1999) 066001 [[hep-th/9901134](#)].
- [68] J. Alanen, E. Keski-Vakkuri, P. Kraus and V. Suur-Uski, *AC Transport at Holographic Quantum Hall Transitions*, *JHEP* **0911** (2009) 014 [[0905.4538](#)].